ABSTRACT

Title of dissertation: NONLINEAR PULSE

PROPAGATION THROUGH

AN OPTICAL FIBER:

THEORY AND EXPERIMENT

Bhaskar Khubchandani, Doctor of Philosophy, 2004

Dissertation directed by: Professor Rajarshi Roy
Department of Physics

Pulse propagation through optical fibers is studied for two different phenomena, (i) the evolution of four-wave-mixing and (ii) the interplay between self- and cross-phase modulation for ultra-short pulses in a polarization maintaining fiber.

For the four-wave-mixing case, we present the results of a study of the dynamical evolution of multiple four-wave-mixing processes in a single mode optical fiber with spatially and temporally δ-correlated phase noise. A nonlinear Schrodinger equation (NLSE) with stochastic phase fluctuations along the length of the fiber is solved using the Split-Step Fourier method. Good agreement is obtained with previous experimental and computational results based on a truncated-ODE model in which stochasticity was seen to play a key role in determining the nature of

the dynamics. The full NLSE allows for simulations with high frequency resolution (60MHz) and frequency span (16THz) compared to the truncated ODE model (300GHz and 2.8THz respectively), thus enabling a more detailed comparison with observations. Fluctuations in the refractive index of the fiber core are found to be a possible source for this phase noise. It is found that index fluctuations as small as 1 part per billion are sufficient to explain observed features of the evolution of the four-wave-mixing sidebands. These measurements and numerical models thus may provide a technique for estimating these refractive index fluctuations which are otherwise difficult to measure.

For the case of self- and cross-phase modulation, the evolution of orthogonal polarizations of asymmetric femtosecond pulses (810nm) propagating through a birefringent single-mode optical fiber (6.9cm) is studied both experimentally (using GRENOUILLE) and numerically (using a set of coupled NLSEs). A linear optical spectrogram representation is derived from the electric field of the pulses and juxtaposed with the optical spectrum and optical time-trace. The simulations are in good qualitative agreement with the experiments. Input temporal pulse asymmetry is found to be the dominant cause of output spectral asymmetry. The results indicate that it is possible to modulate short pulses both temporally and spectrally by passage through polarization maintaining optical fibers with specified orientation and length.

NONLINEAR PULSE PROPAGATION THROUGH AN OPTICAL FIBER : THEORY AND EXPERIMENT

by

Bhaskar Khubchandani

Dissertation submitted to the Faculty of the Graduate School of the
University of Maryland, College Park in partial fulfillment
of the requirements for the degree of
Doctor of Philosophy
2004

Advisory Commmittee:

Professor Rajarshi Roy, Chair/Advisor
Dr. Parvez N. Guzdar, Co-Advisor
Professor Robert W. Gammon
Professor Thomas Antonsen
Professor Edward Ott

ACKNOWLEDGMENTS

I owe my gratitude to all the people who have made this thesis possible and because of whom my graduate experience has been one that I will cherish forever.

First and foremost I'd like to thank my advisor, Professor Rajarshi Roy for giving me an invaluable opportunity to work on challenging and extremely interesting projects over the past four years. He has always made himself available for help and advice and there has never been an occasion when I've knocked on his door and he hasn't given me time. It has been a pleasure to work with and learn from such an extraordinary individual.

I would also like to thank my co-advisor, Dr. Parvez Guzdar. Without his extraordinary theoretical ideas and computational expertise, this thesis would have been a distant dream. Thanks are due to Professor Robert Gammon, Professor Edward Ott and Professor Thomas Antonsen for agreeing to serve on my thesis committee and for sparing their invaluable time reviewing the manuscript.

My colleagues at the nonlinear optics laboratory have enriched my graduate life in many ways and deserve a special mention. David DeShazer helped me start-off by rewriting the basic simulation code in a user-friendly format. Christian Silva provided help by setting up the GRENOUILLE apparatus and performing some

of the simulations. My interaction with Rohit Tripathi, Ryan McAllister, Vasily Dronov, Min-Young Kim, Elizabeth Rogers, William Ray, Jordi Garcia Ojalvo, Riccardo Meucci, Atsushi Uchida, and Fabian Rogister has been very fruitful. I'd also like to thank Wing-Shun Lam and Benjamin Zeff for providing the LaTex style files for writing this thesis.

I would also like to acknowledge help and support from some of the staff members. Donald Martin's technical help is highly appreciated, as is the computer hardware support from Edward Condon, LaTex and software help from Dorothea Brosius and purchasing help from Nancy Boone.

I owe my deepest thanks to my family - my mother and father who have always stood by me and guided me through my career, and have pulled me through against impossible odds at times. Words cannot express the gratitude I owe them. I would also like to thank Dr. Mohan Advani, Dr. Vasudeo Paralikar and Dr. Vinod Chaugule who are like family members to me.

My housemates at my place of residence have been a crucial factor in my finishing smoothly. I'd like to express my gratitude to Sivasankar Pandeti, Jayakumar Patil, Amit Trehan and Punyaslok Purakayastha for their friendship and support.

I would like to acknowledge financial support from the Office of Naval Research (ONR), Physics, for all the projects discussed herein.

It is impossible to remember all, and I apologize to those I've inadvertently left out.

Lastly, thank you all and thank God!

TABLE OF CONTENTS

LIST OF FIGURES

Chapter 1

Introduction

1.1 Source of Nonlinearity in an Optical Fiber

The response of any dielectric to light becomes nonlinear for intense electromagnetic fields. Standard optical fibers are made of fused silica which is a dielectric. The total polarization $\mathbf{P}$ is nonlinear in the electric field $\mathbf{E}$ and is given by [1-5] -

$$\mathbf{P} = \epsilon_0 \left(\chi^{(1)} : \mathbf{E} + \chi^{(2)} : \mathbf{EE} + \chi^{(3)} : \mathbf{EEE} + \ldots \right), \tag{1.1}$$

where ϵ_0 is the permittivity of free-space, and $\chi^{(j)}$ is the j-th order susceptibility of the dielectric. The linear susceptibility $\chi^{(1)}$ represents the dominant contribution to $\mathbf{P}$ and its effects are included through the refractive index $\mathrm{n}(\omega)$ and the attenuation coefficient $\alpha(\omega)$. $\chi^{(2)}$ is responsible for nonlinear effects such as sum-frequency generation and second harmonic generation [1, 3]. Fused silica does not manifest these effects as it is centro-symmetric [6]. Hence, the dominant nonlinear contribution to $\mathbf{P}$ is due to $\chi^{(3)}$ which results in effects such as third harmonic generation, four-wave-mixing, self- and cross-phase modulation. The cubic nonlinearity results in an intensity dependent refractive index

$$\tilde{n}(\omega, |E|^2) = n(\omega) + n_2|E|^2 \tag{1.2}$$

where n(ω) is the linear part given by the Sellmier equation which takes into account the resonance frequencies (ω_j) of fused silica [1, 7],

$$n^2(\omega) = 1 + \sum_{j=1}^{m} \frac{B_j \omega_j^2}{\omega_j^2 - \omega^2} \tag{1.3}$$

and n_2 is given by

$$n_2 = \frac{3}{8n} Re(\chi^3_{xxxx}) \tag{1.4}$$

for an optical wave assumed to be linearly polarized along one of the axes of a polarization maintaining fiber. The tensorial nature of $\chi^{(3)}$ needs to be considered for the case in which the light is not polarized along one of the fiber axes.

The experimentally measured value of n_2 for fused silica ranges from 2.2-3.4 x 10^{-20} m^2/W which is small compared to most other nonlinear media by at least 2 orders of magnitude [1]. Despite this, nonlinear effects are easily observed for silica fibers for relatively low input power levels due to the fact that the effective fiber core areas are small and the fiber losses are low. Single mode fibers (those which propagate a single transverse mode of light for a given wavelength) have effective fiber core diameters of the order of 5μm thus causing the light intensities within the fiber to be large despite the smallness of the input power. The low loss in the fiber (<10 dB/km) allows one to use long fibers to observe nonlinear phenomena.

1.2 Physics of Pulse Propagation

Mathematically speaking, in the classical limit, pulse propagation in an optical fiber is governed by Maxwell's equations [8, 9],

$$\begin{aligned} \vec{\nabla} \times \vec{E} &= -\frac{\partial \vec{B}}{\partial t} \\ \vec{\nabla} \times \vec{H} &= \vec{J} + \frac{\partial \vec{D}}{\partial t} \\ \vec{\nabla} \cdot \vec{D} &= \rho_f \\ \vec{\nabla} \cdot \vec{B} &= 0 \end{aligned} \tag{1.5}$$

where $\vec{E}$ and $\vec{H}$ are electric and magnetic field vectors, and $\vec{D}$ and $\vec{B}$ are electric and magnetic flux densities respectively. $\vec{J}$ is the current density and ρ_f is the free charge density.

Under the following assumptions [8] -

(a) there are no free charges ($\vec{J} = \rho_f = 0$), a good approximation for an optical fiber,

(b) the medium is non-magnetic ($\vec{M} = 0$), which an optical fiber is,

(c) the wavelength of light propagated is away from any material resonances (0.5 - 2 μm), the results described in this thesis lie in this wavelength range, i.e, the results presented in Chapter 2 and Chapter 3 lie in the 600-700 nm regime and the results presented in Chapter 4 lie in the 800 nm regime,

(d) the electric-dipole approximation is valid, due to which the second-order parametric processes such as three-wave-mixing and second harmonic generation can

be neglected (in practice they do occur because of quadrupole and magnetic-dipole effects but with a very low efficiency),

(e) the medium only responds locally, which is a valid approximation for the projects considered herein,

(f) the nonlinear polarization $\vec{P}_{NL}$ can be taken as a perturbation to the total induced polarization $\vec{P}$, which is justified as the nonlinear effects are relatively weak for the results presented in this thesis,

(g) only 3rd order nonlinear effects need to be taken into account, which is valid up to 5th order in $\mathbf{E}$ since the 2nd and 4th order effects are absent due to the centrosymmetric nature of the disordered liquidlike state of fused silica,

(h) the imaginary part of the dielectric constant $\epsilon(\omega)$ is small compared to the real part (low loss, which is a good approximation for the wavelength regimes and fiber lengths considered here),

(i) the wavelength of light is higher than the cutoff wavelength of the fiber so that the single transverse mode condition is satisfied (or else there would be multimode propagation and nonuniform modal dispersion would have to be taken into account),

(j) the optical fiber is polarization maintaining and the light pulse is traveling along one of the 2 principal axes of the fiber, a very good approximation for the results of Chapter 2, and Chapter 3, in the case of Chapter 4, this approximation is relaxed as the incident light travels along both axes of the fiber, thus requiring a set of two coupled NLSEs for simulation, one for each axis,

(k) the slowly varying envelope approximation is valid, i.e., $\Delta\omega/\omega_0 \ll 1$ where $\Delta\omega$ is the spectral width of the pulse spectrum which is centered at ω_0, this approximation

is valid for the studies considered in Chapter 2 and Chapter 4, in Chapter 3, the Raman Stokes wave is considered as a separate slowly varying envelope from the pump wave, as the two taken together would not satisfy this condition,

(l) the nonlinear response of the medium is instantaneous, an approximation valid for pulse widths greater than ∼70 fs, which amounts to neglecting the contribution of molecular vibrations to $\chi^{(3)}$ (the Raman effect), which have been included in the study presented in Chapter 4 since the pulse width was ∼ 140 fs.

the propagation of the slowly varying envelope A(z,t) of a light pulse along an optical fiber is governed by the nonlinear partial differential equation [8] -

$$\frac{\partial A}{\partial z} + \beta_1 \frac{\partial A}{\partial t} + \frac{i\beta_2}{2}\frac{\partial^2 A}{\partial t^2} = i\gamma|A|^2 A, \tag{1.6}$$

where $v_g = 1/\beta_1$ is the group velocity of the pulse, β_2 is the group velocity dispersion coefficient, and γ is the nonlinearity coefficient given by

$$\gamma = \frac{n_2\omega_0}{cA_{eff}} \tag{1.7}$$

Here ω_0 is the central angular frequency of the pulse and A_{eff}, the effective core area of the fiber.

Under transformation to a frame of reference moving at the group velocity of the pulse, the above equation takes the form of the so-called 'nonlinear Schrodinger equation' (NLSE), i.e.

$$\frac{\partial A}{\partial z} + \frac{i\beta_2}{2}\frac{\partial^2 A}{\partial \tau^2} = i\gamma|A|^2 A \tag{1.8}$$

where

$$\tau = t - \frac{z}{v_g} \tag{1.9}$$

is time measured in a frame of reference moving at the group velocity v_g of the pulse.

1.3 Numerical Pulse Propagation

The NLSE, like most nonlinear partial differential equations, is not amenable to analytical solution except in certain special cases where the inverse scattering transform can be used [10]. Thus a numerical approach is necessary for understanding the physics of phenomena governed by the NLSE. The numerical methods available can be classified as finite-difference techniques and pseudo-spectral techniques. Usually pseudo-spectral methods are an order of magnitude faster, the most popular method being the Split-Step Fourier Method (SSFM) [8, 11, 12]. The speed of the SSFM can be partly attributed to the use of the finite fast-Fourier transform (FFT) algorithm [13].For an algorithmic description of the SSFM the reader is referred to Chapter 2, Section 2. Therein is also described an unconditionally stable scheme for including linear multiplicative noise into the SSFM without disturbing the conservative properties of the NLSE. In the projects described in Chapters 3, simulations were carried out using a combination of the SSFM and finite difference schemes. The SSFM is also used to arrive at the simulated results described in Chapter 4.

1.4 Experimental Pulse Diagnostics

With the advent of frequency resolved optical gating (FROG) [14, 15, 16], it has become possible, to not only measure the optical spectrum and optical time trace of a light pulse but to measure the full electric field envelope (intensity and phase) of the light pulse. The two fields of nonlinear fiber optics and frequency resolved optical gating (FROG) are yet to undergo cross pollination to their fullest potential since the inception of FROG 10 years ago. This novel experimental technique adds new dimensions to pulse measurement techniques, one of which is the ability to measure how asymmetric a pulse is, i.e, measure its skewness, kurtosis and all higher order moments. Asymmetric pulse propagation is a subject of interest in Chapter 4, where a highly simplified version of FROG [17] is used to measure pulse characteristics before and after a fiber.

1.5 Group Velocity Dispersion

Group velocity dispersion [18] (GVD) involves the temporal broadening of a pulse as it propagates through an optical fiber. From the NLSE (Eq. 1.6) one can derive length scales relevant to linear dispersion (L_D=T_0^2/β_2) and nonlinearity (L_{NL}=$1/\gamma P_0$). Here T_0 is the pulse width and P_0 is the peak power of the pulse. The regime in which the effects of GVD dominate and the effects of nonlinearity are negligible is given by -

$$\frac{L_D}{L_{NL}} = \frac{\gamma P_0 T_0^2}{|\beta_2|} \ll 1 \tag{1.10}$$

In this regime, optical pulses propagate as they undergo symmetric temporal broadening and linear chirping without any spectral broadening. The sign of the GVD parameter β_2 determines the sign of the induced chirp. If the input pulse is chirped, then it may undergo some initial pulse compression followed by temporal broadening. Unlike the second order dispersion associated with GVD, third order dispersion causes asymmetric temporal broadening with leading and trailing edges. It becomes important, when the operating wavelength is near the zero dispersion wavelength of the fiber (the wavelength at which β_2=0). GVD starts to limit optical fiber communication systems when consecutive pulses broaden so much that they start to overlap.

1.6 Self-Phase Modulation

Self-Phase Modulation [19] (SPM) is a phenomenon that leads to spectral broadening and modulation of optical pulses. In the absence of GVD, SPM induced spectral broadening occurs without change in the temporal pulse shape. The spectral broadening occurs as a consequence of an intensity dependent phase-shift. The project described in Chapter 2 has the property that $L_{NL} < L \ll L_D$, i.e, the nonlinear term representing SPM dominates. In the regime where both SPM and GVD are non-negligible (as in Chapter 4), phenomena qualitatively different from those described in this section and the previous section can occur. Both temporal and spectral broadening can occur simultaneously. In the regime of femtosecond pulse propagation (as in Chapter 4), GVD, third-order dispersion, intrapulse Raman scattering (discussed in Chapter 2) and higher order nonlinear effects have to be taken

into account. If the input pulse is asymmetric, then SPM effects dominate over all other effects, as is observed in Chapter 3. In some cases SPM can lead to pulse compression, and in the anomalous dispersion regime ($\beta_2 < 0$), the balance between GVD and SPM can lead to soliton formation.

1.7 Four-wave-mixing

Four-wave-mixing (FWM) [20] is a parametric process involving the interaction between four photons at different frequencies. Two different kinds of four-wave-mixing processes are possible -

$$\omega_4 = \omega_1 + \omega_2 + \omega_3 \tag{1.11}$$

$$\omega_3 + \omega_4 = \omega_1 + \omega_2 \tag{1.12}$$

The former process results in third harmonic generation for the special case when $\omega_1 = \omega_2 = \omega_3$. Both processes require phase matching to occur, in order to be efficient. For the latter case, with the partial degeneracy of $\omega_1 = \omega_2$, it is relatively easy to satisfy the phase matching condition of

$$\Delta k = k_3 + k_4 - k_1 - k_2 = 0 \tag{1.13}$$

This process is of great interest to nonlinear dynamicists as the evolution of the FWM process could constitute a route to chaos further down-stream in the fiber. It is also of great interest to people working in the field of optical communication

systems, as it can cause cross-talk between neighboring channels in a wavelength division multiplexing scheme of communication.

1.8 Cross-Phase Modulation

Cross-phase modulation (XPM) [21] occurs in optical fibers when two or more optical pulses having different central wavelengths propagate simultaneously inside a fiber, interacting through the fiber nonlinearity which couples the two pulses nonlinearly. The evolution of the two pulses depends on the group velocity mismatch between them by virtue of their being centered at different wavelengths, although this is a linear phenomenon. The group velocity mismatch also exists between light pulses traveling along orthogonal polarization axes of a fiber, and centered around identical wavelengths, since the slow axis and fast axis of the fiber have different group velocities. In this case too, the two polarizations interact nonlinearly [22] through degenerate XPM (degenerate since the central wavelengths are the same). In the case of degenerate XPM the 2nd order and higher dispersion parameters, and the nonlinear parameters (all of which depend only on the wavelength), are also the same unlike in general XPM. The effects of XPM are more pronounced when one of the pulses (the pump) has much higher power than the other (the probe). Otherwise the effects of self phase modulation (SPM) tend to dominate.

1.9 Stimulated Inelastic Scattering

Other nonlinear effects (apart from those due to the cubic $\chi^{(3)}$ nonlinearity) arise due to the interaction between the light traveling in the fiber and the fiber medium.

Interactions between the light field and the vibrational levels of the fiber medium lead to stimulated Brillouin scattering (SBS) and stimulated Raman scattering (SRS). SRS and SBS were among the first nonlinear effects studied in optical fibers [23, 24, 25].In a simple quantum mechanical picture [1] applicable to both SRS and SBS, a photon of the incident field (called the pump) is annihilated to create a photon at a lower frequency (belonging to the Stoke's wave) and a phonon to conserve energy and momentum. SBS involves an acoustic phonon whereas SRS involves an optical phonon, thus they have qualitatively different dispersion relations. SBS has a much lower threshold power and manifest itself through a backward propagating wave in contrast to SRS which can involve both forward and backward traveling waves. SBS has a maximum gain at a frequency 10 GHz [26] (down-shifted with respect to the pump) and requires a very narrow bandwidth pump to manifest itself. SRS, in contrast, has a maximum gain at a frequency 13 THz [27] downshifted with respect to the pump. For pulse-bandwidths larger than 13 THz, the phenomenon of Intrapulse Raman Scattering (IRS) manifests itself, involving a self-frequency shift within the pulse from higher frequency components to lower frequency components. Thus, SRS becomes more important for shorter pulses (larger bandwidth) unlike SBS which nearly ceases to occur for pulses shorter than 10 ns. In both SRS and SBS, the optical fiber plays an active role in the nonlinear process, unlike the case of cross- and self-phase modulation, four-wave-mixing and third harmonic generation, where the fiber plays a passive role by mediating the interaction between several optical waves.

1.10 Outline of Thesis

In Chapter 2, we present the results of a computational study of the influence of stochasticity on the dynamical evolution of multiple four-wave-mixing processes in a single mode optical fiber with spatially and temporally δ-correlated phase noise. A generalized nonlinear Schrodinger equation (NLSE) with stochastic phase fluctuations along the length of the fiber is solved using the Split-step Fourier method (SSFM). Good agreement is obtained with previous experimental and computational results based on a truncated-ODE (Ordinary Differential Equation) model in which stochasticity was seen to play a key role in determining the nature of the dynamics. The full NLSE allows for simulations with high frequency resolution (60 MHz) and frequency span (16 THz) compared to the truncated ODE model (300 GHz and 2.8 THz respectively), thus enabling a more detailed comparison with observations. A physical basis for this hitherto phenomenological phase noise is discussed and quantified.

In Chapter 3, we discuss the implications of spontaneous and stimulated Raman scattering on the project discussed in Chapter 2, namely, the dynamical evolution of stochastic four-wave-mixing processes in an optical fiber. The following question is asked - can stimulated Raman scattering be a mechanism by which adequate multiplicative stochastic phase fluctuations are introduced in the electric field of light undergoing four-wave-mixing as? Adequately checked numerical algorithms of stimulated Raman scattering (SRS), spontaneous Raman generation and intrapulse Raman scattering (IRS) are used while exploring this issue. The algorithms

are described in detail, as also are the results of the simulations. It is found that a 50 meter length of fiber (as used in the experiments), is too short to see the influence of Raman scattering, which is found to eventually dominate for longer fiber lengths.

In Chapter 4, self- and cross-phase modulation (XPM) of femtosecond pulses (810 nm) propagating through a birefringent single-mode optical fiber (6.9 cm) is studied both experimentally (using GRENOUILLE - Grating Eliminated No Nonsense Observation of Ultrafast Laser Light Electric Fields) and numerically (by solving a set of coupled nonlinear Schrodinger equations or CNLSEs). An optical spectrogram representation is derived from the electric field of the pulses and is linearly juxtaposed with the corresponding optical spectrum and optical time-trace. The effects of intrapulse Raman scattering (IRS) are discussed and the question whether it can be a cause of asymmetric tranfer of pulse energies towards longer wavelengths is explored. The simulations are shown to be in good qualitative agreement with the experiments. Measured input pulse asymmetry, when incorporated into the simulations, is found to be the dominant cause of output spectral asymmetry. The results indicate that it is possible to modulate short pulses both temporally and spectrally by passage through polarization maintaining optical fibers with specified orientation and length.

Chapter 5 provides the conclusion to the thesis.

Chapter 2

Stochastic Four-Wave-Mixing

2.1 Overview

The understanding of nonlinear processes in optical fibers is crucial towards extending the capabilities of modern optical communication systems based on wavelength division multiplexing (WDM), where each communication channel is represented by a unique wavelength. One of the nonlinear processes that limits the information carrying capacity of a WDM system is four-wave mixing (FWM), which causes cross-talk between neighboring channels. This places a lower limit on the wavelength separation between adjacent channels and an upper limit on the input power in each channel. In this study, we describe a process by which the evolution of FWM processes in an optical fiber can be used to estimate the inhomogeneities in the fiber core material, in particular the fluctuations in the linear refractive index of the fiber core.

Experiments measuring the evolution of FWM processes along a length of fiber were carried out by Hart et. al. [28] and are described in detail in Section 2.2. In this experiment, two input pump waves at frequencies ω_1 and ω_2, interacted with

each other through the third-order nonlinearity of the fiber material to generate first-order sidebands at frequencies $\omega_3 = 2\omega_1 - \omega_2$ and $\omega_4 = 2\omega_2 - \omega_1$. These waves further interacted to produce second-order sidebands at $\omega_5 = 2\omega_3 - \omega_4$ and $\omega_6 = 2\omega_4 - \omega_3$. Higher-order sidebands were also generated. The normalized power in the sideband at frequency ω_m was represented by ρ_m. The evolution of the FWM processes was characterized by the evolution of ρ_m(z) as a function of fiber length z.

In the present work, we make a quantitative comparison between these experimental results and our numerical results based on efficient algorithms [8] to solve the nonlinear Schrödinger equation (NLSE) that governs the system. The numerical model, its underlying assumptions and the results are described in Section 2.3. A realistic description of a standard single mode optical fiber must take into account the random phase perturbations a light wave undergoes while propagating through it, without disturbing the underlying conservative properties of the system. The NLSE needs to be suitably modified in order to incorporate the stochastic nature of the propagation. In order to preserve the conservative properties of the system, the stochastic terms in the NLSE must necessarily be multiplicative in nature as an additive term acts as a source or a sink. An algorithm that achieves this with linear, Gaussian, δ-correlated noise is outlined in Section 2.3. This algorithm preserves the unconditional stability of the system. At the same time, care is taken to transform the stochastic NLSE from its original Ito representation [29] to the computationally feasible Stratanovich representation [30] by compensating for the spurious linear drift that results from integrating such stochastic differential equa-

tions [31, 32, 33, 34]. The dominant sources of phase noise, are discussed in Section 2.4.

Conclusions on the relevance of the experiments of Hart et. al. [28] and the stochastic modeling presented here are summarized in Section 2.5.

2.2 Experimental and Computational Background

In this work, we focus on tracing the evolution of the sidebands, generated through FWM, along a length of optical fiber. The FWM spectral evolution along 50 m of fiber for two input pump power regimes (2.1 W and 5.5 W) was investigated [28]. In the 2.1 W case, the sideband evolution followed a damped sinusoid along the length of the fiber. The experiments also found that the two first-order sidebands (ρ_3-blueshifted and ρ_4-redshifted from the two pumps) had different evolutions along the fiber (with different spatial wavelengths). For the 5.5 W case, the evolution of both first- and second-order sidebands was measured. The damping in the first-order sidebands (ρ_3 and ρ_4) occured faster than in the 2.1 W case. Experiments probing the dependence of the sideband power on the input power (ranging from 2 W to 17 W) were also performed at a fixed output length of 50 m of the fiber. At the same fiber length, the optical spectra for input powers ranging from 2 W to 17 W were also recorded [28]. The spectral envelopes were observed to fit well to a hyperbolic secant function and the fit parameters were recorded. Measurements with a high-resolution wavemeter showed that one of the two pumps consisted of two very closely spaced longitudinal modes ($\Delta\nu \sim 0.5$ GHz) which were not resolved by the spectrometer used to record the FWM spectra. Inclusion of this multimode

nature of the pump input in their model was found to alter the sideband dynamics dramatically and partly explained the asymmetry between the blueshifted and redshifted sidebands though it did not account for the damping in the sidebands. This was accounted for by adding weak phase fluctuations to the waves as they propagated along the fiber [28]. The physical source of these phase fluctuations was not known at that time. However, the inclusion of the phase fluctuations into the model gave excellent qualitative and quantitative agreement with experiment. Their model involved integration of a system of coupled ODEs derived from the NLSE [35] by a process of truncation that retained only the leading frequency components (the pumps and the first- and second-order sidebands), a process justified by the fact that the input pump waves are well approximated by a combination of monochromatic waves. Their final numerical results are based on simulations using the truncated-ODE model with Langevin noise terms representing phase fluctuations in the fiber. Another physical source of stochasticity in their experiment was the inherent power fluctuation in the lasers used as the input pumps. The level of fluctuations (5-20%) was measured and incorporated appropriately into their model through stochastic initial conditions. This explained the evolution of the level of observed fluctuations in the sideband trajectories although it was found to be inadequate by itself, to account for the damping of the trajectories. They found that all the three physical characteristics mentioned above, namely the multimode nature of the pump input, the stochastic phase fluctuations along the length of the fiber, and the stochastic initial power fluctuations were crucial to explaining the different features of the experimental measurements [28].

2.3 Stochastic NLSE Model

In the present work, we have developed and implemented an unconditionally stable scheme for integrating the NLSE that successfully incorporates phase noise into the SSFM. Thus, we are now in a position to harness, the high frequency / time resolution of the SSFM together with its efficient convergence properties. Due to these advances, we are now able to do simulations with much higher frequency resolution (60 MHz as compared to 300 GHz in the ODE model). This high resolution, coupled with an appropriate convolution scheme enables us to compare these simulated spectra with the composite spectra observed by the spectrometers which had a resolution of $\sim$ 60 GHz. This was not possible with the truncated ODE model as the resolution of the simulated spectra in that case was $\sim$ 300 GHz. For exactly the same levels of phase fluctuations, and initial condition fluctuations as used in Ref.[28], comparisons for the present NLSE model with the experimental sideband evolution functions $\rho_i(z)$ show excellent quantitative agreement. These results, along with the algorithms employed, are described in detail in this section. We have identified linear refractive index fluctuations along the fiber length to be a strong candidate for a physical source of the stochastic phase fluctuations. A comparison between the various possible sources is given in Section 2.4.

Under the assumption that the electric field of the light in the fiber has a slowly varying envelope $A(z, \tau)$, and that the fiber medium has an instantaneous nonlinear response, the system is well described by the nonlinear Schrödinger equation (NLSE) with a linear multiplicative stochastic term

$$\frac{\partial U}{\partial z} + \frac{i\beta^{(2)}}{2T_0^2}\frac{\partial^2 U}{\partial \tau^2} + \frac{\alpha U}{2} + i\Gamma(z,\tau)U - i\gamma P_0|U|^2 U = 0. \tag{2.1}$$

Z is distance along the length of the fiber, $U(z,\tau) = A(z,\tau)/\sqrt{P_0}$ is the complex electric field envelope $A(z,\tau)$ normalized to the absolute amplitude of the field $\sqrt{P_0}$, P_0 is the total power in the fiber, τ is time normalized to a convenient time scale $T_0(\sim 1\ ns)$ measured in a reference frame moving with the group velocity of the pulse $[\tau = (t - z/v_g)/T_0]$. The simulations are carried out for exactly the same physical parameters as the experiments and simulations reported by Hart et. al. [28], i.e. $\beta^{(2)} = 55\ (ps)^2/km$, is the group velocity dispersion of the fiber at the operating wavelength $\lambda_0 \sim 632$ nm ($k_0 \sim 10^7\ m^{-1}$). A loss of ~ 6 dB/km gives $\alpha = 0.0014$ m^{-1} as the loss in the fiber at this wavelength. The nonlinearity coefficient $\gamma = 0.019\ W^{-1}m^{-1}$ is given by

$$\gamma = \frac{\omega_{ave} n_2^I}{cA_{eff}}, \tag{2.2}$$

where A_{eff} is the effective core area of the fiber, n_2^I is the Kerr coefficient for the intensity-dependent refractive index, and ω_{ave} is the average angular frequency of the wave envelope. $\Gamma(z,\tau)$ is a linear multiplicative phase noise field. In this study the noise field is assumed to be δ-correlated in both space and time. The evolution of the FWM dynamics is found to be sensitive to the strength of this noise field. It can be physically interpreted as phase noise arising due to fluctuations in the linear refractive index of the fiber medium. A detailed discussion of its physical origin is

given in Section 2.4.

The system was simulated using the Split-Step Fourier Method (SSFM) [8]. An algorithm for appropriately incorporating stochastic phase fluctuations along the length of the fiber in the SSFM was developed and is summarized below.

The NLSE is composed of linear and nonlinear terms, and can be written in operator form as

$$\begin{aligned} \frac{\partial U}{\partial z} &= (\hat{D} + \hat{S} + \hat{N})U \\ \hat{D} &= \frac{-i\beta^{(2)}}{2T_0^2}\frac{\partial^2}{\partial \tau^2} - \frac{\alpha}{2} \\ \hat{S} &= i\Gamma(z,\tau) \\ \hat{N} &= i\gamma P_0 |U|^2. \end{aligned} \tag{2.3}$$

where $\hat{D}$, $\hat{S}$ and $\hat{N}$ are linear (dispersive), nonlinear and stochastic operators respectively. It has an exact solution for infinitesimal Δz given by -

$$U(z + \Delta z, \tau) = exp[\Delta z(\hat{D} + \hat{S} + \hat{N})]U(z,\tau) \tag{2.4}$$

which can be approximated by

$$U(z + \Delta z, \tau) \approx exp[\Delta z\hat{D}]exp[\Delta z\hat{S}]exp[\Delta z\hat{N}]U(z,\tau) \tag{2.5}$$

The execution of $exp[\Delta z\hat{N}]$ is carried out in τ-space :

$$B_1(z,\tau) = exp[\Delta z\hat{N}]U(z,\tau) \tag{2.6}$$

The execution of $exp[\Delta z\hat{S}]$ and $exp[\Delta z\hat{D}]$ is carried out in ω-space.

In particular, the stochastic phase fluctuations are introduced by modifying the phase ϕ_j of each frequency component ω_j of the complex field according to

$$B_2(z,\omega) = \mathcal{F}[B_1(z,\tau)]$$

$$B_3(z,\omega_j) = exp[i\delta\phi(z,\omega_j)]B_2(z,\omega_j) \tag{2.7}$$

where $\mathcal{F}$ represents the Fourier transform operation.

This process only modifies the phase of each complex frequency component, leaving its absolute value unchanged. Thus the algorithm conserves the total power and the unconditional stability of the system.

The stochastic phase fluctuations $\delta\phi(z,\omega_j)$ are taken to be δ-correlated in frequency as well as spatially along the fiber length. The Box-Muller algorithm [36] was used to generate Gaussian random deviates from computer-generated uniform random deviates r_{1j} and r_{2j} at each spatial step and for each frequency component ω_j. The fluctuations are given by

$$\delta\phi(z,\omega_j) = \sqrt{-2\sigma_\phi^2\Delta z ln(r_{1j})}cos(2\pi r_{2j}) \tag{2.8}$$

This is followed by the execution of $exp[\Delta z\hat{D}]$ which is also carried out in Fourier space, followed by the inverse transform.

$$U(z+\Delta z,\tau) = \mathcal{F}^{-1}[exp[\Delta z\hat{D}(i\omega)]B_3(z,\omega)] \tag{2.9}$$

$\hat{D}(i\omega)$ is obtained by replacing $\frac{\partial}{\partial\tau}$ by $i\omega$.

The basic form of the initial complex wave envelope function is

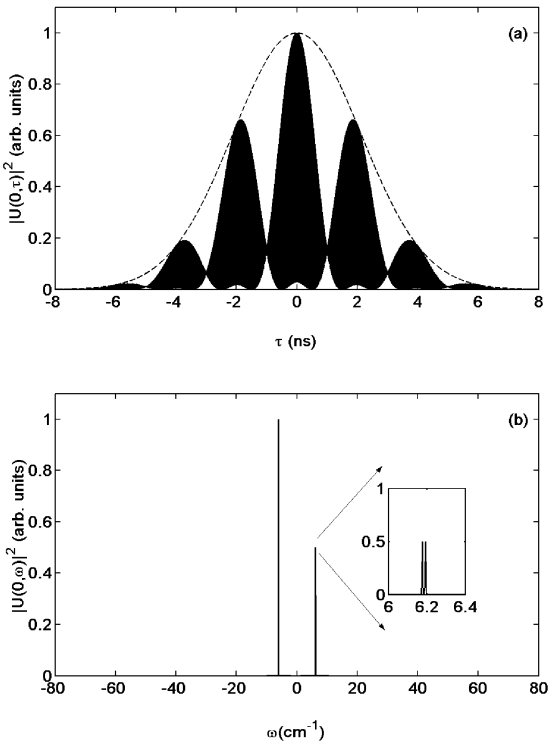

Figure 2.1: Multimode pulse input to the NLSE: (a) input pulse in time domain and (b) input spectrum.

$$U(0,\tau) = exp\left(-\frac{\tau^2}{2\tau_p^2}\right)\left\{\begin{array}{l} exp\left(\frac{i\Omega\tau}{2}\right) + \\ exp\left(-\frac{i\Omega\tau}{2}\right) \end{array}\right\} \tag{2.10}$$

τ_p is the pulse width T_p=5 ns FWHM, normalized to the time scale T_0, Ω=366 GHz is the frequency detuning between the two laser sources normalized to a frequency scale Ω_0=62.5 MHz. Fig. 2.1(a) shows a plot of this pulse $|U(0,\tau)|^2$. The overall Gaussian envelope has an FWHM of 5 ns, the closely spaced dark lines are due to the 366 GHz ($\sim$3 ps) beating between the two input pump frequencies. The 2 ns modulations on the pulse are due to the 0.5 GHz mode-structure in the blue-shifted pump wave. Fig. 2.1(b) shows the input spectrum of this pulse which consists of two highly monochromatic pump waves with a detuning of Ω=366 GHz. The spectrum of the blue-shifted pump, upon magnification, is seen to be composed of two very closely spaced peaks, with a separation of $\Delta\nu$=0.5 GHz. Hart et. al. [28] did not use pulsed wave functions in their NLSE simulations as the size of the FFT required to do so made it computationally prohibitive at that time. The size of the FFT was chosen such that it would accommodate a time span of 16 ns in order to go sufficiently far into the wings on the Gaussian pulse; and a frequency span of 16 THz in order to accommodate all the sidebands generated and prevent spurious effects due to the reflection boundary conditions implicit in the SSFM algorithm. These considerations dictated the size of the FFT to be $\geq$(16 THz)$\cdot$(16 ns)=256000. The nearest power of 2 is 2^{18}=262144, which has been used throughout the present work. The incorporation of the pulsed nature of the light was found to be necessary in explaining the dynamics. From the perspective of the coupled amplitude equations

used by Hart et. al. [28], the present model is equivalent to a coupled-ODE model with 2^{18} coupled ODEs.

Upon incorporation of the multimode nature of the blue input pump laser source and the stochastic fluctuations in the initial power in the lasers, the initial wave function takes the form

$$U(0,\tau) = exp\left(-\frac{\tau^2}{2\tau_p^2}\right)\left\{\begin{array}{l} \sqrt{\frac{1+\delta\rho_1}{2}}\left[\begin{array}{l} exp\left(\frac{i(\Omega+\Delta\nu)\tau}{2}\right)+ \\ exp\left(\frac{i(\Omega-\Delta\nu)\tau}{2}\right) \end{array}\right] \\ +\sqrt{1+\delta\rho_2}exp\left(-\frac{i\Omega\tau}{2}\right) \end{array}\right\}. \tag{2.11}$$

$\Delta\nu$=0.5 GHz is the frequency separation between the two longitudinal modes in the blue-shifted pump. $\delta\rho_1$ and $\delta\rho_2$ are Gaussian random deviates (generated using the Box-Muller algorithm [36]) that represent the initial power fluctuations in each of the pump laser sources. Their standard deviations were taken to be, σ_{ρ_1}=0.2, σ_{ρ_2}=0.11 for simulations from 0 m to 20 m, σ_{ρ_1}=0.12, σ_{ρ_2}=0.05 for simulations from 20 m to 50 m along the length of the fiber. This is exactly the same prescription used by Hart et. al. [28] in their simulations and is dictated by their experimental measurements of the fluctuations in the pump laser intensities.

At this point it is worth noting the effects of the inclusion of two attributes of the input laser light, namely the multimode nature of the blueshifted pump, and the pulsed nature of the input light (assumed to be cw in the simulations reported by Hart et. al. [28]).

Figure 2.2 shows a comparison between simulations with (solid curves) and without (dashed curves) the multimode nature for an input pump power of 2.1

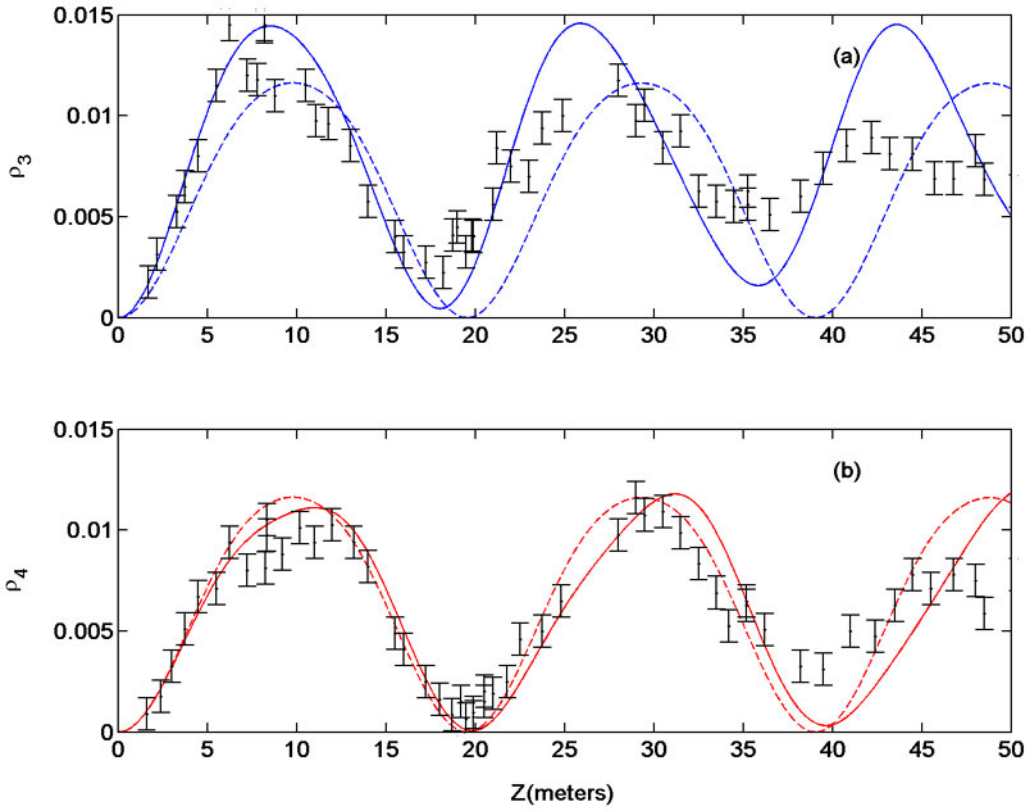

Figure 2.2: Effects of inclusion of the multimode nature ($\Delta\nu$=0.5 GHz) of the blueshifted input pump laser on the 1st order sideband evolution as a function of fiber length for P_0=2.1W. Dashed curves represent simulations without the multimode nature and solid curves represent simulations with the multimode nature. Ω=366 GHz, γ=0.019$W^{-1}m^{-1}$, and $\beta^{(2)}$=55ps^2/km (a) power in the blueshifted sideband, (b) power in the redshifted sideband

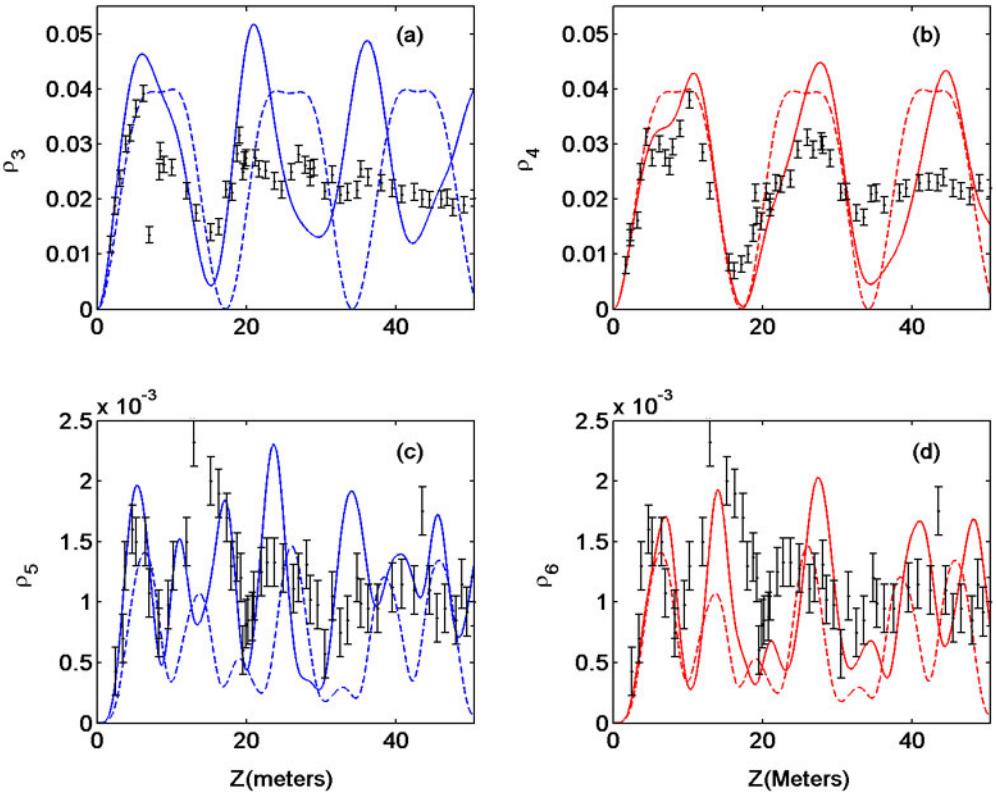

Figure 2.3: Effects of inclusion of the multimode nature ($\Delta\nu$=0.5 GHz) of the blueshifted input pump laser on the 1st order sideband evolution as a function of fiber length for P_0=5.5W. Dashed curves represent simulations without the multimode nature and solid curves represent simulations with the multimode nature. Ω=366 GHz, γ=0.019$W^{-1}m^{-1}$, and $\beta^{(2)}$=55ps^2/km (a) power in the 1^{st} order blueshifted sideband, (b) power in the 1^{st} order redshifted sideband, (c) power in the 2^{nd} order blueshifted sideband, (d) power in the 2^{nd} order redshifted sideband

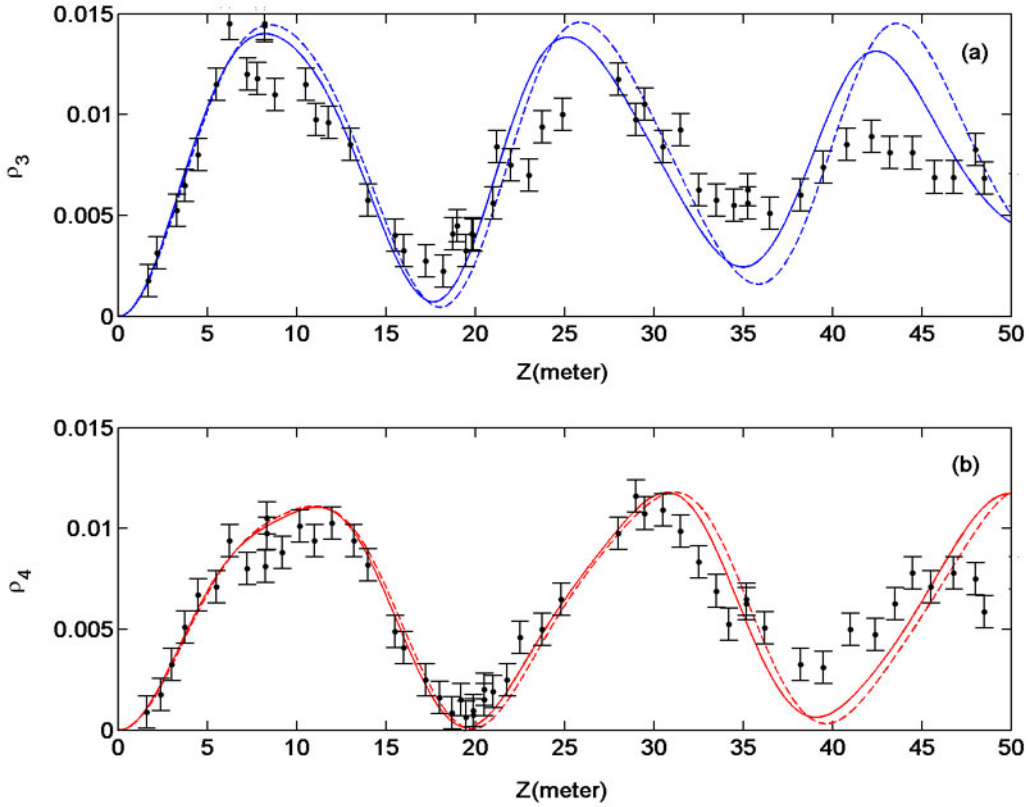

Figure 2.4: Effects of inclusion of the pulsed nature (5 ns FWHM) of the input pump laser light on the 1st order sideband evolution as a function of fiber length for P_0=2.1W. Dashed curves represent cw simulations and solid curves represent pulsed simulations. Ω=366 GHz, $\Delta\nu$=0.5, γ=0.019W^{-1}m^{-1}, and $\beta^{(2)}$=55ps^2/km (a) power in the blueshifted sideband, (b) power in the redshifted sideband

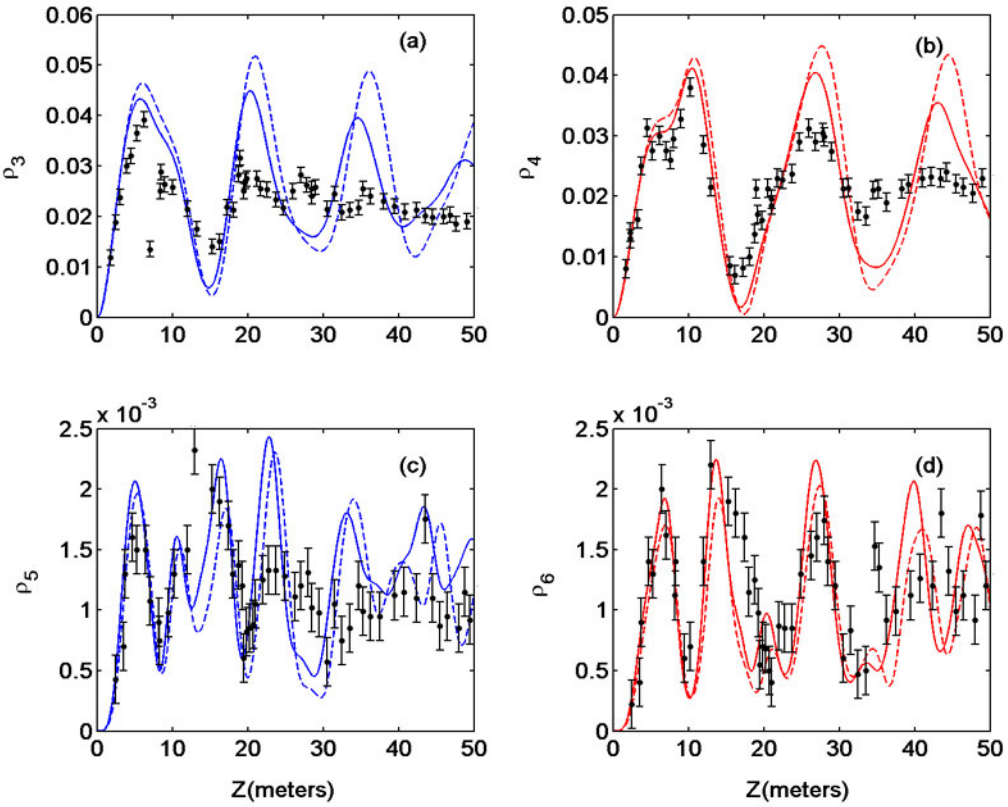

Figure 2.5: Effects of inclusion of the pulsed nature (5 ns FWHM) of the input pump laser on the 1st and 2nd order sideband evolution as a function of fiber length for P_0=5.5W. Dashed curves represent cw simulations and solid curves represent pulsed simulations. Ω=366 GHz, $\Delta\nu$=0.5, γ=0.019W^{-1}m^{-1}, and $\beta^{(2)}$=55ps^2/km (a) power in the 1^{st} order blueshifted sideband, (b) power in the 1^{st} order redshifted sideband, (c) power in the 2^{nd} order blueshifted sideband, (d) power in the 2^{nd} order redshifted sideband

Watts. The simulations with the mode structure show the asymmetry between the blue- and red-shifted sideband evolution, in particular, the difference in spatial wavelength between the two, and a non-return to zero nature of the evolution, as observed in the experimental data (black dots with error bars). These features are absent in the simulations without mode-structure. ρ_3 and ρ_4 stands for the first order blue- and red-shifted sidebands respectively. Figure 2.3 shows the corresponding comparison for the case of 5.5 Watts of input pump power. Here too, the simulations incorporating the multimode nature of the blueshifted pump (solid curves) are seen to be an improvement over those not incorporating it (dashed curves). A feature of the experimental data (black dots with errorbars) is that for the ρ_3 sideband, the initial part of the evolution involves a peak followed by a shoulder, while for the ρ_4 sideband, the initial part of the evolution involves a shoulder followed by a peak. This feature too is seen to occur as a result of the inclusion of the multimode nature of the blueshifted pump.

The effect of inclusion of the pulsed nature of the input beam is seen in figure 2.4 (for the 2.1 Watt case) and figure 2.5 (for the 5.5 Watt case). The solid dashed represent simulations for a cw input beam and the solid curves represent those for a pulsed input beam. The incorporation of the pulsed nature clearly results in damping of the sideband trajectories which are seen to come closer to the experimental data [28] (black dots with error bars).

Use of the FFT algorithm makes evaluation relatively fast compared to other finite-difference schemes. The computational error is $O(\Delta z^2)$, thus the solution converges with decreasing spatial step-size Δz.

The simulations were tested for the conservation of total power along the fiber length (by setting the loss α to zero) and for the conservation of asymmetry [35, 28] given by

$$C(Z) = \sum_{i=1}^{\infty} (2i-1)[\rho_{2i-1}(Z) - \rho_{2i}(Z)] \tag{2.12}$$

A clearer picture of the evolution of the sidebands is obtained by plotting both, the power in the sidebands, and their standard deviations as a function of length along the fiber. Figures 2.6(a) and 2.6(b) show a comparison between simulation and experiment, of the evolution of the first-order blueshifted (ρ_3) and redshifted (ρ_4) sidebands respectively, for an input power of 2.1 W. The dashed curves represent NLSE simulations which include the stochastic nature of the input powers of the pump lasers but exclude the stochastic phase fluctuations added along the length of the fiber, an attribute which is included in the simulations represented by the solid curves. The black dots with error bars represent the experimental data. The measured sideband power, normalized to the total power in the fiber, is periodic in length, but appears to be damping to a constant value. The measured data also show a clear difference between the spatial wavelengths of oscillation of the blueshifted (ρ_3) and redshifted (ρ_4) sidebands trajectories respectively. Both these features are captured well by both the simulations. Figures 2.6(c) and 2.6(d) compare experimental and simulated measures of the evolution of the standard deviation in the sideband power along the fiber length. It is clearly observed that simulations with phase noise added to the light field along the length of the fiber

(solid curves) are closer to the experimental data as compared to those that exclude this feature (dashed curves). This indicates the instrumental nature of the phase fluctuations in explaining key features of the dynamics.

The apparent damping of the periodic sideband trajectory is seen more dramatically in figures 2.7(a) and 2.7(b), which show the evolution of the first-order sideband power along the fiber for an input power of 5.5 W. The two first-order sidebands evolve differently. They appear to damp to a constant value at a faster rate than for the case with an input pump power of 2.1 W. Here again, NLSE simulations that incorporate phase noise along the length of the fiber (solid curves) are much more successful in accurately capturing the dynamical features of the system than NLSE simulations that do not take this feature into account (dashed curves). Figures 2.7(c) and 2.7(d) show a comparison between the simulated and measured standard deviations. Comparisons for the second-order blueshifted (ρ_5) and redshifted (ρ_6) sidebands, respectively, are shown in figures 2.7(e) and 2.7(f).

The observed dynamical evolution of the sidebands is found to depend sensitively on the strength of the stochastic phase fluctuations. Yet, best agreement with the experimental results of Hart et. al. [28] is achieved with exactly the same noise strength σ_ϕ^2 as used in their truncated ODE model, namely σ_ϕ^2=0.0067 m^{-1}. They report that including phase noise in their FWM calculations resulted in a spurious linear drift in the trajectories for the sideband power with length. To remove this artifact of the computations, they added a linear loss to their coupled ODEs. They set the loss coefficient α=0.0046 m^{-1} by finding the value that removed this increasing slope. We have observed exactly the same secular growth phenomenon for a

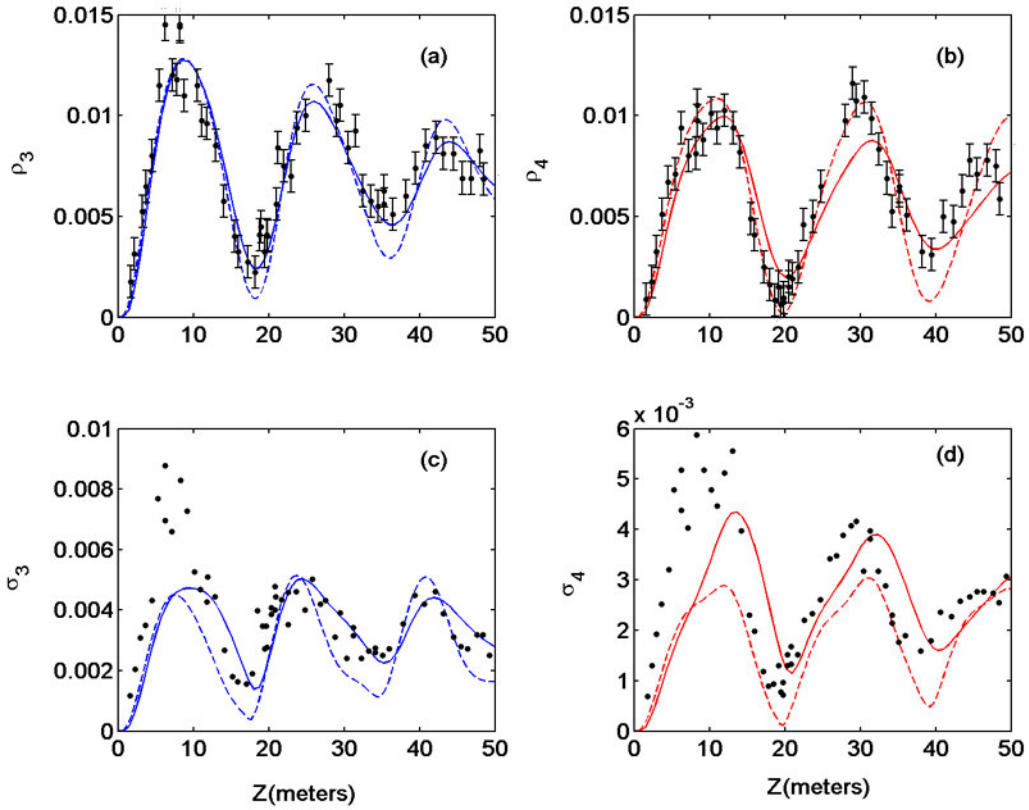

Figure 2.6: Comparison between the experimental measurements [28](black), the random initial condition NLSE model excluding phase noise (dashed curves) and the stochastic phase noise NLSE model (solid curves) showing the 1st order sideband evolution as a function of fiber length for P_0=2.1W, Ω=366 GHz, $\Delta\nu$=0.5 GHz,γ=0.019$W^{-1}m^{-1}$, and $\beta^{(2)}$=55ps^2/km: dynamical evolution of the: (a) power in the blueshifted sideband, (b) power in the redshifted sideband, (c) fluctuations in the blueshifted sideband, (d) fluctuations in the redshifted sideband

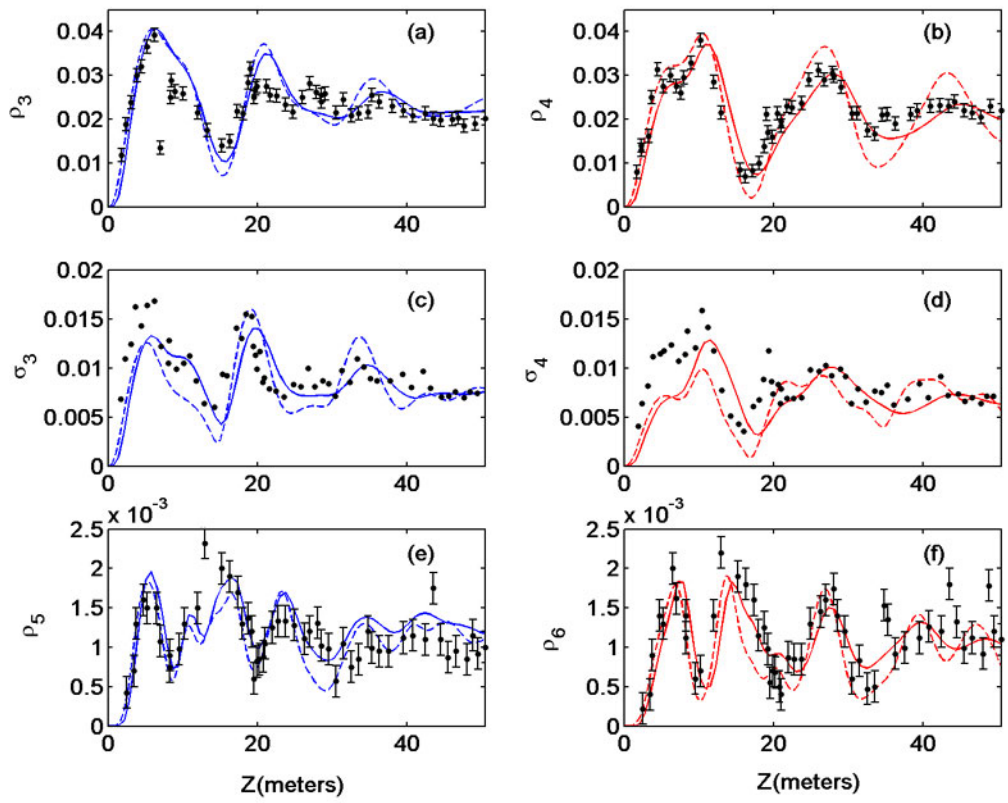

Figure 2.7: Comparison between the experimental measurements [28] (black), the random initial condition NLSE model excluding phase noise (dashed curves) and the stochastic phase noise NLSE model (solid curves) showing the 1st and 2nd order sideband evolution as a function of fiber length for P_0=5.5W, Ω=366 GHz, $\Delta\nu$=0.5 GHz,γ=0.019$W^{-1}m^{-1}$, and $\beta^{(2)}$=55ps^2/km: dynamical evolution of the: (a) power in the 1^{st} order blueshifted sideband, (b) power in the 1^{st} order redshifted sideband, (c) fluctuations in the 1^{st} order blueshifted sideband, (d) fluctuations in the 1^{st} order redshifted sideband, (e) power in the 2^{nd} order blueshifted sideband, (f) power in the 2^{nd} order redshifted sideband

wide range of the noise strength σ_ϕ^2 and have arrived at an empirical prescription for α namely, $\alpha \sim \sigma_\phi^2$, where σ_ϕ^2 is the variance of the added phase noise. This indicates the general nature of dynamics resulting from the addition of stochastic, δ-correlated phase fluctuations to systems governed by nonlinear partial differential equations [31].

It is remarkable that the strength of the phase noise required is the same in both the 2.1 W and the 5.5 W cases. Further, it is worth noting that exactly the same noise strength was used by Hart et. al. [28], the difference being that they introduced phase noise only in the pump frequencies, whereas we have introduced it in all the Fourier modes ($\sim 2^{18}$). As a confirmation of this result, they also performed experiments and numerical simulations examining the sideband power dependence on the input power at a fixed length of 50.4 m of the same fiber. We have repeated these simulations with the stochastic NLSE model and the results are shown in figures 2.8(a) (blueshifted sideband) and 2.8(b) (redshifted sideband). The experimental measurements of the sideband powers are represented by filled squares and the results of numerical simulations are represented by triangles (without phase noise) and by circles (with phase noise). The simulations are seen to follow the general trend seen in the experiments. As the pump power is increased, the triangles (without phase noise) start to disagree with experiment, whereas the circles (with phase noise) are much closer to experiment. The phase noise strength used in these simulations was exactly the same as that used in the simulations depicted in figures 2.6 and 2.7. The agreement between the phase noise simulations and the experimental data was (once again) highly sensitive to the noise strength. Since

this experiment (unlike those shown in figures 2.2 - 2.7) is non-destructive, it can be used to deduce the strength of phase noise processes in a given optical fiber. It will be shown in Section 2.4 that a likely cause of the phase noise is fluctuation in the linear refractive index of the fiber. The noise strength deduced from the present computational study corresponds to a refractive index inhomogeneity of $\langle \Delta n^2 \rangle \sim 10^{-16}$.

Till now the comparisons between our simulations of the full NLSE and the truncated ODE model give basically the same results, although with much better agreement with experiment. However, the full NLSE can also provide a detailed comparison with the experimental spectra. This was not available from the truncated ODE model. The simulations reported in this work were carried out with a very high frequency and time resolution in order to incorporate the fact that the input light was not cw, but was composed of ~ 5 ns long pulses; and that the number of sidebands generated required the frequency spread of the FFT to be ~ 16 THz, while resolving a longitudinal mode-structure of $\Delta\nu \sim 0.5$ GHz. The spectral resolution used was ~ 0.05 GHz, whereas the spectrometer used to observe the spectra had a resolution 1000 times larger (~ 50 GHz). To account for this difference, the simulated spectra were first convolved with a Gaussian of unit peak and 62GHz FWHM, before they were compared with the observed spectra.

Figures 2.9(a) and 2.9(b) show three-dimensional plots of the average experimental FWM output spectrum along the length of the fiber for input pump powers of 2.1 W and 5.5 W respectively (courtesy Hart et. al. [28]). The vertical axis represents the intensity, normalized to the peak power in one of the input pumps,

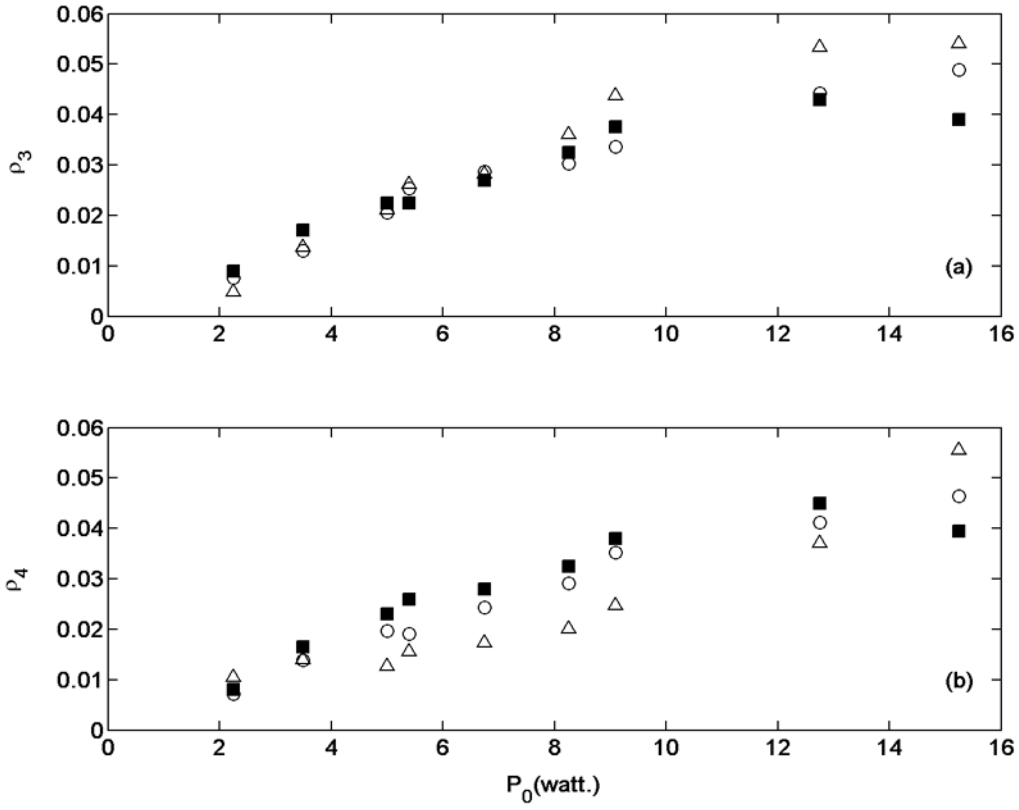

Figure 2.8: Comparison between the experimental measurements (filled squares), simulations without stochastic phase fluctuations (open triangles) and with stochastic phase fluctuations (open circles) of the first order sideband power versus pump input power for L=50.39 m, and Ω=366 GHz: power in the (a) blueshifted sideband and (b) redshifted sideband.

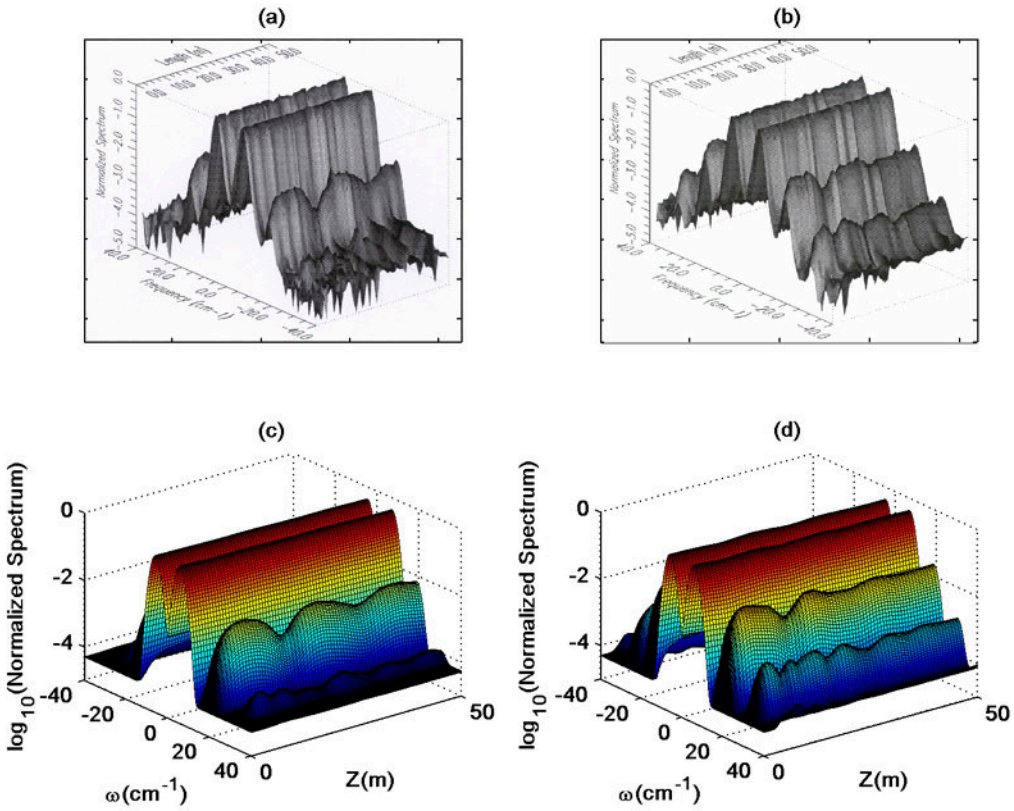

Figure 2.9: Evolution of the FWM spectrum along the fiber (a) P=2.1 W, experiment, (b) P=5.5 W, experiment, (c) P=2.1 W, stochastic-NLSE model, (d) P=5.5 W, stochastic-NLSE model

plotted on a logarithmic scale. The pump frequencies are centered on $+/-\Omega/2$ and the fiber length is increasing into the page. Figures 9(c) and 9(d) show the corresponding comparisons based on simulations using the stochastic-NLSE model. The basic features of the spectral evolution are captured by the simulations.

Hart et. al. [28] also documented the experimentally observed FWM output spectra for a fixed fiber length of 50.39 meters for 6 different input pump powers. They state the coefficients A and B of the hyperbolic secant envelopes that best fit the output spectra which are given by

$$f(\omega) = Asech(B\omega) \tag{2.13}$$

where A and B are the experimental fit parameters.

The hyperbolic secant parameters A and B, that best fit the simulated spectra are exactly the same as those that best fit the experimental spectra [28] for all the 6 cases of input power considered. Fig. 2.10 shows an overlap of the simulated spectra (dashed line), with the experimental spectra (solid line) and the experimental hyperbolic secant envelope (dotted line) for 6 different pump powers, namely, (a) 2.1W, (b) 5.5W, (c) 6.7W, (d) 8.3W, (e) 12.7W, (f) 17.4W. The hyperbolic secant parameters for each of these pump powers are (a)A=3.85 and B=0.36, (b)A=2.26 and B=0.27, (c)A=1.81, B=0.25, (d)A=1.56 and B=0.23, (e)A=0.98,B=0.20, and (f)A=0.81 and B=0.20. The exact shapes of the simulated spectra match very well with the experimental spectra for low input pump powers (2.1W and 5.5W), but tend to lack the "filled-in" character of the experimental spectra at higher powers

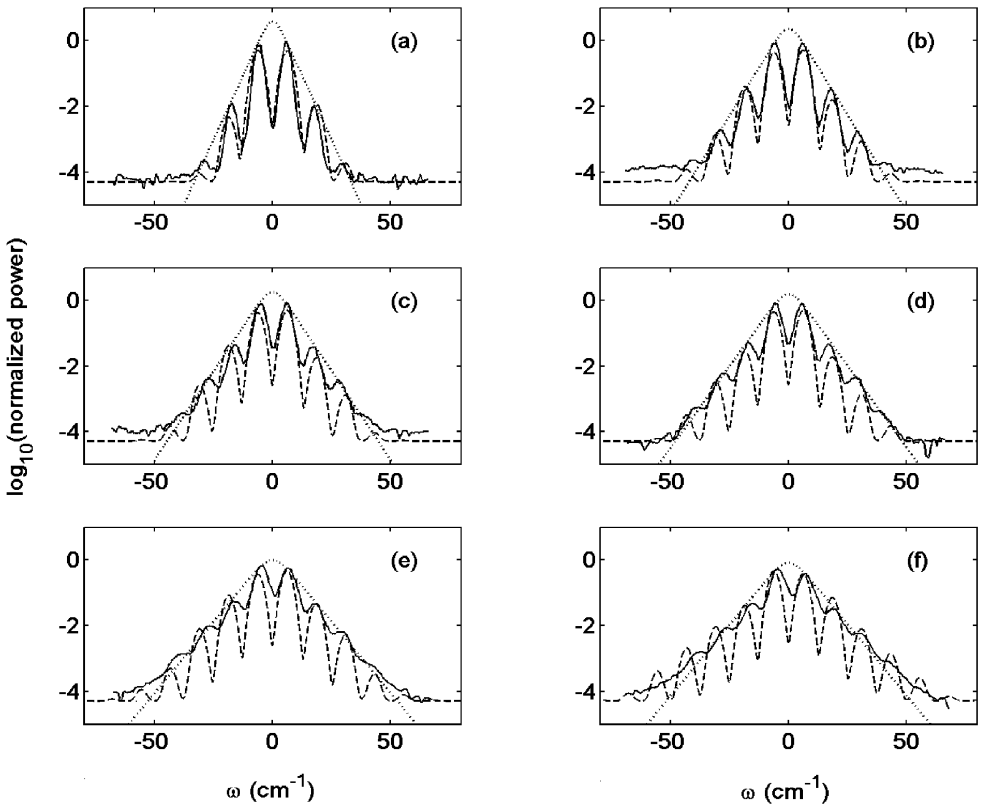

Figure 2.10: Experimental FWM output spectrum (solid line), convolved spectra from simulations of the stochastic NLSE model (dashed line), and hyperbolic secant envelope fit (dotted line) for pump input powers P_0 of (a) 2.1 W, (b) 5.5 W, (c) 6.7 W, (d) 8.3 W, (e) 12.7 W, (f) 17.4 W, fiber length L=50.39m, Ω=366 GHz, $\Delta\nu$=0.5 GHz,γ=0.019W^{-1}m^{-1}, and $\beta^{(2)}$=55ps^2/km

(6.7W, 8.3W, 12.7W and 17.4W).

2.4 Discussion

Hart. et. al. [28] postulated that strong candidates for the possible physical sources of the phase fluctuations are stimulated Brillouin scattering, stimulated Raman scattering and fiber medium inhomogeneities. Brillouin scattering was eliminated as a source, since a backward propagating wave, which is a signature of Brillouin scattering in optical fibers, was not observed in the experiments. We have modeled stimulated Raman scattering [27, 37] for our system and have found no evidence to support the hypothesis that it could be a possible source of the stochastic phase fluctuations for fiber lengths upto 50 meters and pump power levels upto 5.5 Watts. A more detailed discussion of the Raman scattering simulations performed is given in Chapter 3. Apart from these, quantum phase fluctuations are another well known, though extremely weak, source of phase noise in optical fibers [8, 38].

Fiber medium inhomogeneities were identified as the major cause of the stochastic phase fluctuations. These inhomogeneities can manifest themselves through spatial and/or temporal fluctuations in the fiber parameters, namely, the linear refractive index n_0, the group velocity v_g, the group velocity dispersion $\beta^{(2)}$ and the nonlinearity γ [39]. Of these, the fluctuation in the linear refractive index was found to be the only source of phase fluctuation that had a significant effect on the dynamics. A relationship between the level of refractive index fluctuations and the corresponding level of phase fluctuations has been arrived at. It is found that refractive index fluctuations as small as $\sigma_n^2 \sim 10^{-17} m^{-1}$ can cause the desired phase

fluctuations. Possible sources of these refractive index fluctuations are discussed below.

Consider the modified nonlinear Schrödinger equation (NLSE) which is stated below, with the linear multiplicative noise term represented in terms of spatial and temporal fluctuations in the refractive index of the fiber.

$$\frac{\partial U}{\partial z} + \frac{i\beta^{(2)}}{2T_0^2}\frac{\partial^2 U}{\partial \tau^2} + \frac{\alpha U}{2} + ik_0\delta n(z,\tau)U - i\gamma P_0|U|^2U = 0 \tag{2.14}$$

$\delta n(z,\tau)$ is the spatial and temporal variation of the refractive index along the fiber. It can be caused by temperature and density fluctuations in the fiber [40].

The thermodynamic estimate for Δn is given by [40]

$$\langle \Delta n^2 \rangle = \frac{-kT\rho^2}{V^2}\left(\frac{\partial V}{\partial P}\right)_T \left(\frac{\partial n}{\partial \rho}\right)_T^2 + \frac{kT^2}{\rho V C_v}\left(\frac{\partial n}{\partial T}\right)_\rho^2 \tag{2.15}$$

This gives the mean-square index fluctuation in terms of the properties of the material. It can be rewritten as

$$\langle \Delta n^2 \rangle = \frac{V_\rho + V_T}{V} = \langle \Delta n^2 \rangle_\rho + \langle \Delta n^2 \rangle_T \tag{2.16}$$

For a fiber of length z=1m and radius r=2.82μm (Volume V=2.5x10^{-12} m^3), these have been calculated to be -

$$\begin{aligned} \langle \Delta n^2 \rangle_\rho &\sim 10^{-21} \equiv \langle \Delta \rho^2 \rangle \sim 10^{-14}\frac{kg^2}{m^6}, \\ \langle \Delta n^2 \rangle_T &\sim 10^{-23} \equiv \langle \Delta T^2 \rangle \sim 10^{-12}\ {}^oC^2 \end{aligned} \tag{2.17}$$

It should be noted that $\langle \Delta n^2 \rangle \propto \frac{1}{z} \Rightarrow \delta n \propto \frac{1}{\sqrt{z}}$. The corresponding phase fluctuation that this would lead to in the NLSE is given by $\delta\phi = k_0 \delta n z \propto \sqrt{z}$ which is equivalent to the prescription for incorporating phase fluctuations into the stochastic NLSE model described in Section 2.3, namely, $\langle \Delta\phi^2 \rangle = 6.7 \times 10^{-3} z$. Hart et. al. [28] used the same prescription and the same noise strength in their truncated-ODE model. From this we can estimate the level of refractive index fluctuation that corresponds to the noise strength used in the simulations described in Section 2.3 -

$$\begin{aligned} \langle \Delta n^2 \rangle &= \frac{6.7 \times 10^{-3}}{k_0^2} = 6.78 \times 10^{-17} \\ \equiv \langle \Delta T^2 \rangle &\sim 10^{-6}\ {}^{o}C^2 \equiv \Delta T \sim 10^{-3}\ {}^{o}C \end{aligned} \tag{2.18}$$

The temperature coefficient of the refractive index of silica [40], $\left(\frac{\partial n}{\partial T}\right)_\rho \sim 10^{-5}\ {}^{o}C^{-1}$. Thus even small spatio-temporal temperature fluctuations of $\sim 10^{-3}\ {}^{o}C$ are enough to cause the inferred level of refractive index fluctuations.

The refractive index fluctuations could also be due to inhomogeneities in the density of the fiber material, frozen in at the time of manufacture of the fiber. The simulations were averaged over ~ 600 iterations to get a good estimate of the power fluctuations in the sidebands. Initially, simulations were performed with a different phase noise distribution for each iteration. Later, a particular (arbitrary) phase noise distribution was selected and frozen for all the iterations. This did not reduce the level of damping observed in the sideband trajectories provided that the strength of the phase noise was kept the same, thus indicating that density fluctuations induced

during fiber manufacture could be a possible source. The phase noise was modeled as δ-correlated in both space and time. A more realistic approach would be to use correlated noise. Numerical methods to incorporate linear multiplicative correlated noise into the NLSE have been developed by M.J. Werner et. al. [32].

2.5 Conclusions

The role of stochasticity in the dynamical evolution of four-wave-mixing processes in an optical fiber has been investigated. This research consisted of theoretical and numerical computations. It focuses on tracing the evolution of the sidebands, generated through FWM, along a length of optical fiber. Detailed comparisons were made with the experimental results of Hart et. al. [28] and the agreement was excellent. The present work uses numerical techniques that have much higher resolution and better efficiency, and it presents a theoretical basis for the role of the stochasticity in the dynamics. The system is known to be governed by the nonlinear Schrödinger equation (NLSE) to a very good approximation [8].

A powerful technique that can be used for simulations of the stochastic NLSE is the Split-step Fourier Method (SSFM) [8]. An algorithm for the direct implementation of stochastic processes along the length of the fiber in the SSFM has been developed. The advantages of this approach with respect to the coupled-ODE approach are that we can carry out simulations with much higher frequency and time resolution without sacrificing computational efficiency.

The physical sources of these stochastic phase fluctuations are investigated quantitatively and are identified to be due to fluctuations in the linear refractive

index of the fiber. Strong candidates for the causes of these refractive index fluctuations are temperature fluctuations in the fiber medium caused by the fluctuating temperature of the fiber environment, density fluctuations in the fiber medium frozen into the fiber during manufacture, and intrinsic thermodynamic fluctuations in the temperature and density of the fiber.

The experiments performed by Hart et. al. [28] can be used to determine the level of these refractive index fluctuations in commercial fibers. Results described in figures 2 and 3 represent a destructive experiment that measures the sideband evolution with fiber length for a fixed input pump power, necessarily requiring the fiber to be cut repeatedly. The level of refractive index fluctuations can be used as a parameter in the simulations to best fit the experimental results. Alternatively, fig. 4 represents a non-destructive experiment that measures the sideband evolution with input pump power for a fixed fiber length. These experiments are found to be effective for estimating the refractive index fluctuations, as the dynamics is observed to be sensitively dependent on the strength of the phase fluctuations.

Chapter 3

Influence of Raman Scattering

3.1 Introduction

For the stochastic four-wave-mixing project discussed in Chapter 2, it was initially postulated by Hart et. al. [28] that stimulated Raman scattering (SRS) would play a dominant role in explaining the observed dynamics.

This postulate has been explored numerically with the models for simulating Raman scattering available to us [8, 27, 37]. So far we have observed that stimulated Raman scattering does cause phase fluctuations, but the fluctuations are too weak to cause macroscopic fluctuations in the dynamical evolution of the four-wave-mixing. It has also been found that for power levels larger than those used, as well as for fiber lengths longer than those used by Hart et. al. [28], Raman scattering plays a dominant role in governing the nature of the dynamics. In this chapter, the exact method by which stimulated Raman scattering was incorporated into the nonlinear Schrodinger equation (NLSE) approach is discussed in details, along with the results arrived at.

3.2 Simulations Involving a Stokes Seed

The first model used to simulate SRS in the four-wave-mixing scenario is the one described in Ref. [27]. It involved two coupled NLSEs (CNLSEs), one for the pump wave and one for the Stokes wave, which was assumed to be downshifted in frequency from the pump by 13.2 THz [27]. The equations that describe the model are given below -

$$\begin{aligned} \frac{\partial U_p}{\partial z} + \frac{i\beta_{2p}}{2}\frac{\partial^2 U_p}{\partial T^2} &= i\gamma_p(|U_p|^2 + 2|U_s|^2) - \frac{g_p}{2}|U_s|^2 U_p \\ \frac{\partial U_s}{\partial z} + d\frac{\partial U_s}{\partial T} + \frac{i\beta_{2s}}{2}\frac{\partial^2 U_s}{\partial T^2} &= i\gamma_s(|U_s|^2 + 2|U_p|^2) + \frac{g_s}{2}|U_p|^2 U_s \end{aligned} \tag{3.1}$$

where U is the slowly varying envelopes of the electric field, subscripts p and s stand for the pump wave and Stokes wave respectively. As in the single NLSE framework in chapter 1, $\beta_{2p,s}$ and $\gamma_{p,s}$ stand for the group velocity dispersion (GVD) and nonlinearity respectively, of the fiber at the pump/Stokes central wavelength. Similarly, $g_{p,s}$ is the Raman gain coefficient $\sim 1.6 \times 10^{-13}$ m/W (632 nm), T is time measured in a reference frame moving at the group velocity v_{gp} of the pump pulse, and d $\sim$ 4 ps/m (632 nm), is the walk-off parameter [27].

$$T = t - z/v_g, d = v_{gp}^{-1} - v_{gs}^{-1} \tag{3.2}$$

where v_{gp} is the group velocity of the Stokes pulse.

The relationship between the fiber parameters at the pump/Stokes wavelengths is as follows -

$$\beta_{2s} = r\beta_{2p}, \gamma_s = r\gamma_p, g_s = rg_p \tag{3.3}$$

where r=λ_p/λ_s

Each equation is of the general form -

$$\frac{\partial U_i}{\partial z} = (\hat{D}_i + \hat{N}_i + \hat{G}_i)U_i \qquad \text{i=p,s} \tag{3.4}$$

where $\hat{D}$ is a linear dispersive operator, $\hat{N}$ is a nonlinear operator, and $\hat{G}$ is the Raman-gain operator.

$$\hat{D}_p = \frac{i\beta_{2p}}{2}\frac{\partial^2}{\partial T^2}, \hat{D}_s = -d\frac{\partial}{\partial T} + \frac{i\beta_{2s}}{2}\frac{\partial^2}{\partial T^2}$$
$$\hat{N}_p = i\gamma_p(|U_p|^2 + 2|U_s|^2)U_p, \hat{N}_s = i\gamma_s(|U_s|^2 + 2|U_p|^2)U_s$$
$$\hat{G}_p = +g_p|U_s|^2U_p, \hat{G}_s = -g_s|U_p|^2U_s \tag{3.5}$$

A modified split-step-Fourier method is used to solve these equations. The operation of $\hat{D}$ and $\hat{N}$ is carried out in a way similar to that used for solving the single NLSE in Chapter 1. The operation of $\hat{G}$ is carried out by making use of the fact that the quantity $C = r|U_p|^2 + |U_s|^2$ is conserved by these equations. Diagnostic tests involving comparisons with Ref. [27], pg 324-326 were carried out successfully.

The 3 steps of the Split-Step Fourier Method (SSFM) are executed in the following way -

(1) Linear Dispersive Operator $\hat{L}$ -

$$\frac{\partial U_p}{\partial z} + \frac{i\beta_{2p}}{2}\frac{\partial^2 U_p}{\partial T^2} = 0$$
$$\frac{\partial U_s}{\partial z} + d\frac{\partial U_s}{\partial T} + \frac{i\beta_{2s}}{2}\frac{\partial^2 U_s}{\partial T^2} \tag{3.6}$$

Split-Step (1) in Fourier space -

$$U_p(\omega, z+h) = U_p(\omega, z)exp[\frac{i\beta_{2p}}{2}\omega^2 h]$$
$$U_s(\omega, z+h) = U_s(\omega, z)exp[-id\omega h + \frac{i\beta 2s}{2}\omega^2 h] \tag{3.7}$$

(2) Nonlinear Operator $\hat{N}$ -

$$\frac{\partial U_p}{\partial z} = i\gamma_p(|U_p|^2 + 2|U_s|^2)U_p$$
$$\frac{\partial U_s}{\partial z} = i\gamma_s(|U_s|^2 + 2|U_p|^2)U_s \tag{3.8}$$

Split-Step (2) in t-space (since $|(U_p|^2$ and $|U_s|^2$ are constants for this step) -

$$U_p(z+h) = U_p(z)exp[i\gamma_p(|U_p(z)|^2 + 2|U_s(z)|^2)h]$$
$$U_s(z+h) = U_s(z)exp[i\gamma_s(|U_s(z)|^2 + 2|U_p(z)|^2)h] \tag{3.9}$$

(3) Raman Gain Operator $\hat{G}$ -

$$\frac{\partial U_p}{\partial z} = \frac{-g_p}{2}|U_s|^2 U_p$$
$$\frac{\partial U_s}{\partial z} = \frac{+g_p}{2}|U_p|^2 U_s \tag{3.10}$$

Split-Step (3) in t-space

$$U_p(z+h) = U_p(z)\left[\frac{C}{r|U_p(z)|^2 + |U_s(z)|^2 exp[C\gamma_p h]}\right]^{1/2}$$
$$U_s(z+h) = U_s(z)\left[\frac{C}{|U_s(z)|^2 + r|U_p(z)|^2 exp[-C\gamma_p h]}\right]^{1/2} \quad (3.11)$$

where $C = r|U_p(z)|^2 + |U_s(z)|^2$

In order to check the model, we proceeded to try and reproduce the results in Ref. [27] where the equations are rewritten in a dimensionless form by incorporating the relevant length scales in the problem, namely, the walk-off length L_W, the dispersion length L_D, the nonlinear length L_{NL}, and the Raman gain length L_G which are defined in the following fashion :-

$$L_D = \frac{T_0^2}{|\beta_{2p}|}, L_W = \frac{T_0}{|d|}, L_{NL} = \frac{1}{\gamma_p P_0}, L_G = \frac{1}{g_p P_0} \quad (3.12)$$

Length z', time τ and $U_{p,s}$ are non-dimensionalized in the following way -

$$z' = \frac{z}{L_W}, \tau = \frac{T}{T_0}, U_j = \frac{U_j}{\sqrt{P_0}} \quad (3.13)$$

where $T_0 \sim 1$ ps, $f_R \sim 0.18$ [8]

$$\frac{\partial U_p}{\partial z'} + \frac{i}{2}\frac{L_W}{L_D}\frac{\partial^2 U_p}{\partial \tau^2} = \frac{iL_W}{L_{NL}}[|U_p|^2 + (2-f_R)|U_s|^2]U_p - \frac{L_W}{2L_G}|U_s^2 U_p$$
$$\frac{\partial U_s}{\partial z'} - \frac{\partial U_s}{\partial \tau} + \frac{ir}{2}\frac{L_W}{L_D}\frac{\partial^2 U_s}{\partial \tau^2} = \frac{irL_W}{L_{NL}}[|U_s|^2 + (2-f_R)|U_p|^2]U_s + \frac{rL_W}{2L_G}|U_p|^2 U_s \quad (3.14)$$

The following dimensionless numbers are used to specify the parameters of the CNLSE with $\lambda_p = 1.06\mu$m,

$r = \lambda_p/\lambda_s$=0.95, L_D/L_W = 1000, L_W/L_{NL}=24, and L_W/L_G=12

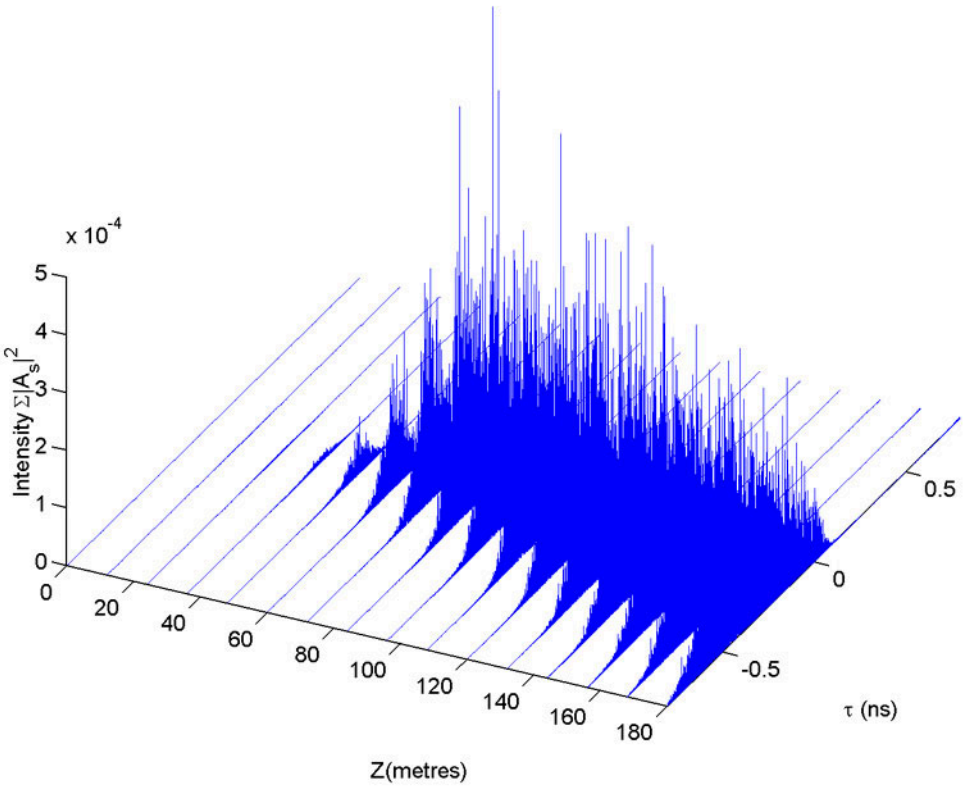

Figure 3.1: Stokes pulse generating from noise and subsequently amplifying and walking off with respect to the reference pump pulse. P_0=5.5W, g_p=0.0094 $W^{-1}m^{-1}$, d=4.1885 ps/m, Ω=366 GHz, $\Delta\nu$=0.5 GHz,γ=0.019$W^{-1}m^{-1}$, and $\beta^{(2)}$=55ps^2/km

The pump pulse is taken to be a Gaussian, while the Raman seed is obtained from

$$A_s(0,T) = \left(P_{s0}^{eff}\right)^{1/2}, P_{s0}^{eff} = 2 \times 10^{-7} W \tag{3.15}$$

The parameters of this model were modified to simulate the four-wave-mixing scenario. It should be noted that the model is completely deterministic and is

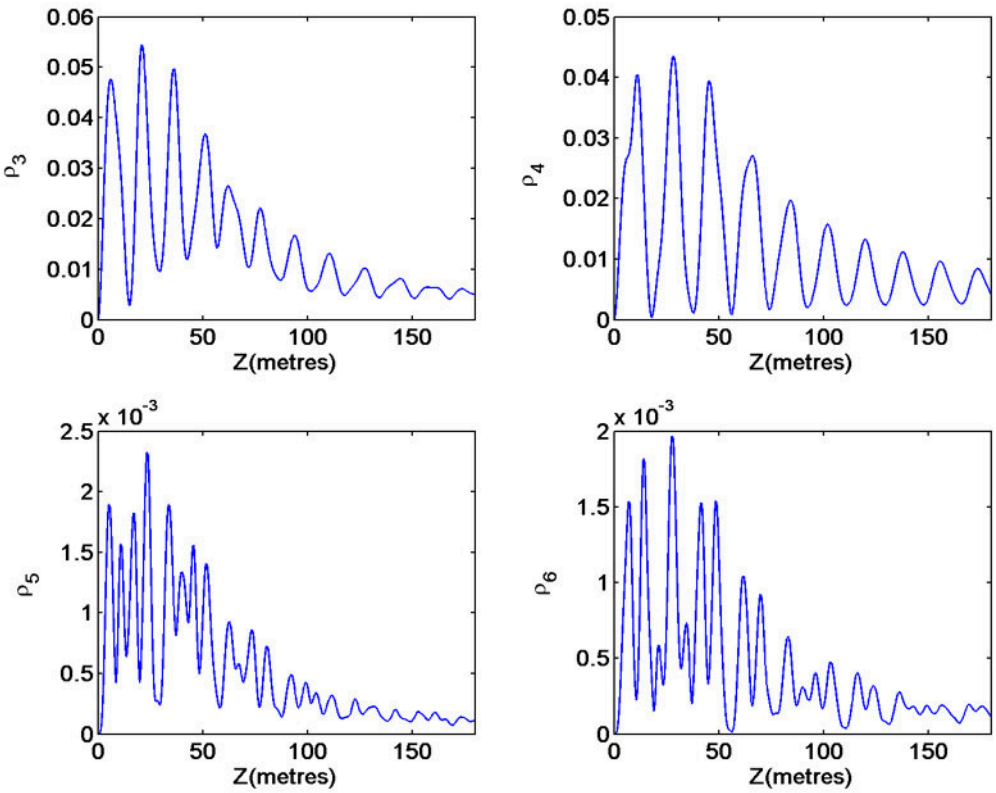

Figure 3.2: 1st and 2nd order sideband evolution as a function of fiber length showing pump depletion as a result of Raman amplification for P_0=5.5W, g_p=0.0094 $W^{-1}m^{-1}$, d=4.1885 ps/m, Ω=366 GHz, $\Delta\nu$=0.5 GHz,γ=0.019$W^{-1}m^{-1}$, and $\beta^{(2)}$=55ps^2/km: dynamical evolution of the: (a) power in the 1st order blueshifted sideband, (b) power in the 1st order redshifted sideband, (c) power in the 2nd order blueshifted sideband, (d) power in the 2nd order redshifted sideband

unlikely to provide any stochasticity to the system. One way to modify the model and introduce stochasticity is to use a Stokes seed pulse which has random intensities and phases. For realistic values of the Raman gain ($\sim 1.6\times10^{-13}$ m/W, the sideband evolution is unaffected. Neither are any fluctuations characteristic of phase noise effects [28] observed nor is any damping of the sideband trajectories observed. When the gain is increased by orders of magnitude, the only effect observed is that of sideband power decay and a monotonic rise in Stokes power, i.e. pump power loss and Stokes power gain. No Stokes wave was observed in the experiments. It was speculated that without a visible Stokes wave (or with a stable Stokes wave containing three orders of magnitude lesser power than the pump wave), there could be exchanges of light between the Stokes and the pump waves thus providing phase noise and damping in the pump sidebands. This was not the case with the results of the simulations.

An example of the results of the Raman incorporated four-wave-mixing simulations is given in figures 3.1 and 3.2. Figure 3.1 shows the build up of the Stokes pulse from noise, and its subsequent walk-off (with respect to the pump pulse, which is chosen as the reference). The noisy input had spectral content with an FWHM bandwidth of 13.2 THz, corresponding to the Raman gain bandwidth for standard silica optical fibers [27]. Figure 3.2 shows the effect of the Raman amplification on the sideband trajectories for the P_0=5.5 Watt case. There is no noticeable effect upto 50 meters (the length upto which the experiment was performed), but the trajectories show a rapid decay over the range of 50 to 150 meters. The quantity $C = r\Sigma|U_p(z)|^2 + \Sigma|U_s(z)|^2$ is observed to be conserved.

Preliminary investigations showed that the effect of pump depletion due to Raman amplification became more significant as the input pump power (or the fiber length) and the input Stokes power were increased. The above scheme is capable of simulating Raman amplification when a weak Stokes signal pulse is injected together with the pump pulse. The coupled NLSEs need to be modified to suitably include a noise term in order to model the case in which the Raman pulse builds up from a zero initial condition (spontaneous Raman generation), exchanges phase noise with the pump pulse and concurrently undergoes Raman amplification (stimulated Raman scattering).

The following is a model [37] that incorporates a noise exchange mechanism between the Stokes and the pump wave into the CNLSE equations :-

$$\begin{aligned}
\frac{\partial U_p}{\partial z} + \frac{i\beta_{2p}}{2}\frac{\partial^2 U_p}{\partial T^2} &= i\gamma_p(|U_p|^2 + 2|U_s|^2)U_p - \frac{g_p}{2}|U_s^2 U_p \\
&\quad + iU_s \int_{-\infty}^{\infty} H_p(\omega + \Omega_R) f_N(z,\omega) e^{-\omega T} d\omega \\
\frac{\partial U_s}{\partial z} + d\frac{\partial U_s}{\partial T} + \frac{i\beta_{2s}}{2}\frac{\partial^2 U_s}{\partial T^2} &= i\gamma_s(|U_s|^2 + 2|U_p|^2)U_s + \frac{g_s}{2}|U_p|^2 U_s \\
&\quad + iU_p \int_{-\infty}^{\infty} H_p(\omega - \Omega_R) f_N^*(z,-\omega) e^{-i\omega T} d\omega
\end{aligned} \tag{3.16}$$

Here H(ω) is the spectral density of the Stokes pulse, and $\Omega_R = \omega_p - \omega_s$ is the frequency difference between the pump and the Stokes pulse. f_N(z,t) is a stationary stochastic function of time defined for all t in the interval -T/2 to T/2. and $\tilde{f}_N(z,\omega)$ is its Fourier transform.

In the preceding equation, the terms that cause Raman generation are -

$$\frac{\partial U_p}{\partial z} = \frac{iU_s f_1(z)}{2}$$
$$\frac{\partial U_s}{\partial z} = \frac{iU_p f_2(z)}{2} \tag{3.17}$$

where $f_1(z)$ and $f_2(z)$ are given by

$$f_1(z) = \int_{-\infty}^{\infty} H_p(\omega + \Omega_R)\tilde{f}_N(z,\omega)e^{-i\omega t}d\omega$$
$$f_2(z) = \int_{-\infty}^{\infty} H_P(\omega - \Omega_R)\tilde{f}_N^*(z,-\omega)e^{-i\omega t}d\omega \tag{3.18}$$

Even for these processes $C = r|U_p|^2 + |U_s|^2, r = \frac{\lambda_p}{\lambda_s}$ is conserved. This implies that $f_1(z)$ and $f_2(z)$ are conjugates of each other with a multiplicative r, i.e.

$$r f_1^*(z) = f_2(z) \tag{3.19}$$

The proof of the above statement is as follows -

Equations (4.17) imply that

$$U_p^* \frac{\partial U_p}{\partial z} = \frac{iU_s U_p^* f_1(z)}{2}$$
$$U_p \frac{\partial U_p^*}{\partial z} = \frac{-iU_s^* U_p f_1^*(z)}{2}$$
$$U_s^* \frac{\partial U_s}{\partial z} = \frac{iU_p U_s^* f_2(z)}{2}$$
$$U_s \frac{\partial U_s^*}{\partial z} = \frac{-iU_p^* U_s f_2(z)}{2} \tag{3.20}$$

in terms of which, the rate of change of the conserved quantity $C = r|U_p|^2 + |U_s|^2$, with respect to fiber length is given by

$$\frac{\partial C}{\partial z} = \frac{1}{2}\left(irU_sU_p^*f_1(z)) - irU_s^*U_pf_1^*(z) + iU_pU_s^*f_2(z) - iU_p^*U_sf_2^*(z)\right) \tag{3.21}$$

Since C is constant with fiber length, the derivative should be zero. This is possible only if $rf_1^*(z) = f_2(z)$.

The numerical algorithm for the Split-Step used to solve equations 4.17 is as follows (to 1^{st} order in Δz) :-

$$\begin{aligned} U_p(z_0+\Delta z) &= U_p(z_0) + \frac{i\Delta z}{4}\left[U_s(z_0)f_1(z_0) + U_s(z_0+\Delta z)f_1(z_0+\Delta z)\right] \\ U_s(z_0+\Delta z) &= U_s(z_0) + \frac{i\Delta z}{4}\left[U_p(z_0)f_2(z_0) + U_p(z_0+\Delta z)f_2(z_0+\Delta z)\right] \end{aligned} \tag{3.22}$$

and to 2^{nd} order in Δz -

$$\begin{aligned} &U_p(z_0+\Delta z) = U_p(z_0) + \tfrac{i\Delta z}{4}U_s(z_0)f_1(z_0) + \\ &\tfrac{i\Delta z}{4}f_1(z_0+\Delta z)\left[\, U_s(z_0) + \tfrac{i\Delta z}{4}\left(\begin{array}{l} U_p(z_0)f_2(z_0) + \\ \\ U_p(z_0+\Delta z)f_2(z_0+\Delta z) \end{array}\right)\right] \end{aligned} \tag{3.23}$$

which is equivalent to -

$$\begin{aligned} &U_p(z_0+\Delta z)[1 + \tfrac{(\Delta z)^2}{16}f_1(z_0+\Delta z)f_2(z_0+\Delta z)] = \\ &U_p(z_0)[1 - \tfrac{(\Delta z)^2}{16}f_1(z_0+\Delta z)f_2(z_0)] + \\ &\tfrac{i\Delta z}{4}U_s(z_0)[f_1(z_0) + f_1(z_0+\Delta z)] \end{aligned} \tag{3.24}$$

Similarly, the 2^{nd} order split-step for U_s is

$$
\begin{aligned}
&U_s(z_0+\Delta z)[1+\tfrac{(\Delta z)^2}{16}f_1(z_0+\Delta z)f_2(z_0+\Delta z)] = \\
&U_s(z_0)[1-\tfrac{(\Delta z)^2}{16}f_2(z_0+\Delta z)f_1(z_0)]+ \\
&\tfrac{i\Delta z}{4}U_p(z_0)[f_2(z_0)+f_2(z_0+\Delta z)]
\end{aligned} \tag{3.25}
$$

The 2 split-steps can be expressed in short-hand notation in the following way -

$$
\begin{aligned}
U_p(z_0+\Delta z) &= A_{11}U_p(z_0)+A_{12}U_s(z_0) \\
U_s(z_0+\Delta z) &= A_{21}U_p(z_0)+A_{22}U_s(z_0)
\end{aligned} \tag{3.26}
$$

where A_{11}, A_{12}, A_{21} and A_{22} are given by -

$$
\begin{aligned}
A_{11} &= \frac{1-\frac{\Delta^2}{16}f_1(z_0+\Delta z)f_2(z_0)}{D} \\
A_{12} &= -\frac{i\Delta[f_1(z_0+f_1(z_0+\Delta z)]}{4D} \\
A_{21} &= \frac{i\Delta[f_2(z_0)+f_2(z_0+\Delta Z]}{4D} \\
A_{22} &= \frac{1-\frac{\Delta^2}{16}f_2(z_0+\Delta z)f_1(z_0)}{D}
\end{aligned} \tag{3.27}
$$

where D is given by -

$$
D = 1-\frac{\Delta^2}{16}f_1(z_0+\Delta z)f_2(z_0+\Delta z) \tag{3.28}
$$

The above model was first checked with the results quoted by Headley et. al. [37] and the results presented therein were reproduced. The evolution of the total Stokes power with fiber length was observed to fluctuate in a stochastic way, as seen

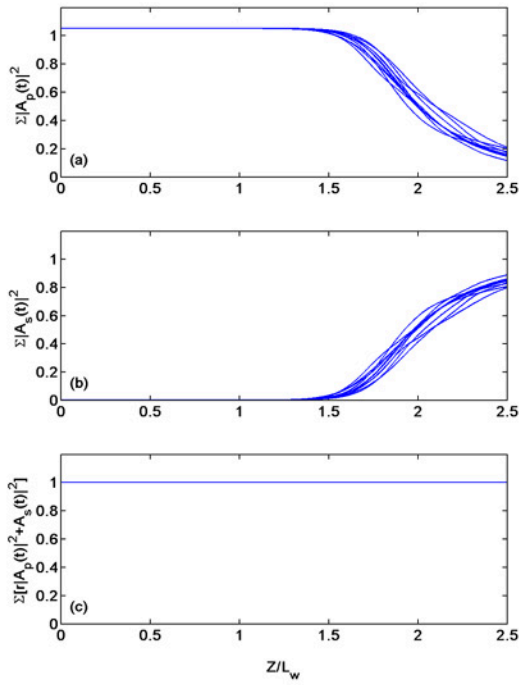

Figure 3.3: Variation of the total (a) pump and (b) Stokes powers and (c) the conserved quantity $C = r\Sigma|U_p(z)|^2+\Sigma|U_s(z)|^2$ with fiber length. Several trajectories are plotted in order to display the stochastic nature of the evolution. The parameters used are L_w/L_g=19.145, L_w/L_{NL}=41.4, L_w/L_D=3.175×10^{-3}

in figure 3.3 (a). All the Stokes power trajectories (figure 3.3(a)) were observed to be monotonically increasing with fiber length, and all the total pump energy trajectories (figure 3.3(b)) were observed to be monotonically decreasing with fiber length. Thus there was no macroscopic mutual exchange of energy between the pump wave and the Stokes wave. The conserved quantity $C = r\Sigma|U_p(z)|^2+\Sigma|U_s(z)|^2$ was observed to be conserved (as seen in figure 3.3(c)). The parameters used for this simulation are L_w/L_g=19.145, L_w/L_{NL}=41.4, L_w/L_D=3.175$\times 10^{-3}$. The corresponding parameters for the four-wave-mixing scenario are L_w/L_g=50, L_w/L_{NL}=125,L_w/L_D=2$\times 10^{-6}$.

The simulations were repeated for the four-wave-mixing parameters and the results are as follows- A Raman pulse was observed to generate from nothing (no initial condition for the Stokes pulse) and to walk-off with respect to the pump pulse (due to a difference in the group velocities of the pump and Stokes pulses). Even though the mechanism for exchange of phase noise exists in the equations, no fluctuation or damping were observed in the sidebands. Yet again, Raman amplification was accompanied by pump depletion and decay and even this effect was negligible for the physical Raman gain parameter of the system over the fiber length of interest (50 meters).

Thus, with the models available, the hypothesis that stimulated Raman scattering is an adequate source of phase fluctuations to result in the damping and fluctuation in sideband evolution, was nullified.

There is one point that deserves to be made about the present framework of simulating SRS in optical fibers. The Stokes pulse is 13.2 THz down-shifted from the pump pulse. However, the full width of the array used to represent the pump and the

Stokes pulses was required to be at least 16 THz (in order to prevent ringing artifacts at the pulse boundaries in the pump four-wave-mixing spectrum. Therefore, there is a 2.8 THz overlap between the simulated pump spectrum and the Stokes spectrum respectively. This fact has not been incorporated into the simulations.

3.3 Intrapulse Raman Scattering

For broadband optical pulses (pulse width $\leq$ 1ps or bandwidth $\geq$ 1 THz), the Raman gain can amplify the low-frequency components of a pulse by transferring energy from the high-frequency components of the same pulse, a phenomenon referred to as the self-frequency shift [8].

$$\begin{aligned} &\tfrac{\partial A}{\partial z} + \tfrac{\alpha}{2}A + \beta_1 \tfrac{\partial A}{\partial t} + \tfrac{i\beta_2}{2}\tfrac{\partial^2 A}{\partial t^2} - \tfrac{\beta_3}{6}\tfrac{\partial^3 A}{\partial t^3} \\ &= i\gamma\left(1 + \tfrac{i}{\omega_0}\tfrac{\partial}{\partial t}\right)\left(A(z,t)\int_{-\infty}^{\infty} R(t')|A(z,t-t')|^2 dt'\right) \end{aligned} \tag{3.29}$$

where R(t) is the nonlinear response function of the medium, normalized such that $\int_{-\infty}^{\infty} R(t)dt = 1$.

The response function should include both the electronic (which is nearly instantaneous) and vibrational (Raman) contributions :-

$$R(t) = (1 - f_R)\delta(t) + f_R h_R(t) \tag{3.30}$$

where f_R represents the fractional contribution of the delayed Raman response function $h_R(t)$. Attempts have been made to determine the approximate analytic form of the Raman response function. A useful form is given by [61]

$$h_R(t) = \frac{\tau_1^2 + \tau_2^2}{\tau_1 \tau_2^2} exp(-t/\tau_2) sin(t/\tau_1) \tag{3.31}$$

The parameters τ_1 and τ_2 have been found (by best fitting the actual Raman gain spectrum) to be τ_1=12.2 fs and τ_2=32 fs [61] f_R has been estimated to be about 0.18 [62, 61, 63].

For pulses shorter than 5 ps (or bandwidth greater than 200 GHz) but longer than 10 fs (wide enough to contain many optical cycles), the slowly varying envelope approximation

$$|A(z, t - t')|^2 \approx |A(z, t)|^2 - t' \frac{\partial}{\partial t} |A(z, t)|^2 \tag{3.32}$$

can be used. Defining the first moment of the nonlinear response function as

$$T_R \equiv \int_{-\infty}^{\infty} tR(t)dt = f_R \int_{-\infty}^{\infty} th_R(t)dt \tag{3.33}$$

and noting that $\int_{-\infty}^{\infty} R(t)dt = 1$, the generalized NLSE takes the form

$$\frac{\partial A}{\partial z} + \frac{\alpha}{2} A + \frac{i\beta_2}{2} \frac{\partial^2 A}{\partial T^2} - \frac{\beta_3}{6} \frac{\partial^3 A}{\partial T^3} = i\gamma \left(|A|^2 A + \frac{i}{\omega_0} \frac{\partial}{\partial T} (|A|^2 A - T_R A \frac{\partial |A|^2}{\partial T} \right) \tag{3.34}$$

where time T is measured in a reference frame moving at the group velocity $T = t - z/v_g \equiv t - \beta_1 z$ of the pulse. Among the three terms in parenthesis on the right hand side of the equation, the first term represents the electronic contribution to nonlinearity, the second term is the self-steepening (SS) term, and the last term is the intrapulse Raman scattering (IRS) term.

The split-step for the intrapulse Raman scattering (IRS) term involves looking at the following equation -

$$\frac{\partial A}{\partial z} = -i\gamma T_R \frac{\partial |A|^2}{\partial T} A \tag{3.35}$$

the numerical solution of which can be split into -

$$\left.\frac{\partial |A|^2}{\partial T}\right|_{T=T(i)} = \frac{|A(z,T(i+1))|^2 - |A(z,T(i))|^2}{T(i+1) - T(i)}$$
$$A(T(i), z+\Delta z) = A(z) exp\left(-i\gamma T_R \left.\frac{\partial |A(z,T)|^2}{\partial T}\right|_{T=T(i)}\right) \tag{3.36}$$

Simulations were initially carried out to test the model by reproducing the simulated results presented in Ref. [64], Chapter 5, page 170. The experimental spectra and spectrograms obtained in the cross-phase modulation experiment described in Chapter 3 showed a transfer or pulse energies towards longer wavelengths, a phenomenon characteristic of IRS.

Intrapulse Raman scattering (IRS) was found to have no visible effect on the dynamical evolution of the four-wave-mixing processes discussed in detail in Chapter 2. However, the effect was found to be clearly noticeable for input pump powers larger than 50 Watts (an order of magnitude higher than the powers that the experiments presented). A clear amplification of the redshifted sidebands and a corresponding depletion of the blueshifted sidebands was observed for this case.

3.4 Conclusion

For the four-wave-mixing project discussed in chapter 2 of this thesis, it has been found that the input pump powers are too low, and the fiber length too small for the effects of SRS to be noticeable. Hart et. al. [28] had postulated SRS to be a possible cause of some of the important dynamical features of the system considered, among them being the stochastic phase fluctuations added to the electric field of the light along the length of the fiber. It is found that while SRS does lead to stochastic phase fluctuations, these fluctuations are too weak to have any noticeable effect for the pump powers and fiber lengths considered. For larger powers, and longer fibers, it is found that the Stokes pulse monotonically (although stochastically) grows in energy, monotonically (and stochastically) depleting the pump wave. A mutual macroscopic exchange of energy between the Stokes and the pump waves has not been observed for the simulations described in this chapter.

Chapter 4

Asymmetric Femtosecond Pulse Propagation

4.1 Overview

The study of ultrashort pulse propagation through optical fibers is highly promising as the applications towards communications, medical and other technologies are widespread. Some of the possible applications include pulse shaping (both spectral and temporal), the encoding of multiple bits of information on a single light pulse, and the spectral and temporal modulation of light pulses. Ultrashort pulses are ideal for this purpose, as they are broadband (10-100 nm), and the commercially available sources usually come in high repetition rate configurations ($\sim$ 100 MHz).

Traditional ways of characterizing ultrashort pulses, such as the intensity autocorrelator, which are unable (in particular) to measure pulse asymmetry, have been superseded by more recent methods. These methods have the ability to not only measure the asymmetry of ultrashort pulses, but to measure the full electric field of the pulses, including the optical intensity and the optical phase. One such method is Frequency Resolved Optical Gating (FROG) [41].

FROG has been used as a measurement technique in the field of nonlinear fiber

optics [42] by several groups. In the regime of wavelengths covered by the mode-locked Ti:Sapphire laser ($\sim$ 810 nm, which lies in the normal dispersion regime of fused silica), such measurements have been carried out notably by Dudley, et. al. [43] for analyzing the broadband continuum generated by femtosecond pulse propagation through a photonic crystal fiber. Dudley et. al. [43] also present results of numerical simulations showing agreement with experiments. In the present work, we discuss experimental and computational results for a polarization maintaining fiber made of fused silica. The advantages are that the refractive index of fused silica is well characterized, making it easier to model the experiments with a pseudospectral nonlinear Schrödinger equation based approach [8]. Moreover, a polarization maintaining fiber was used to avoid the random polarization fluctuations that would result if a standard fiber (non-polarization maintaining) were to be used. This made the study of both self- and cross-phase modulation between orthogonal polarizations possible.

Degenerate cross-phase modulation has been studied extensively in the past [44, 45, 46] where asymmetric spectral broadening has been reported and well explained. More recently, other groups have studied the evolution of femtosecond pulse propagation through fused silica fibers using FROG in the 1.3 μm and the 1.55 μm regime, notable among them being the works of Omenetto et. al. [47, 48, 49], Nishizawa et. al. [50, 51, 52, 53] and Ogawa et. al. [54]. The works of Nishizawa et. al. involve the study of cross-phase modulation in optical fibers using FROG. In particular, the effects of input pulse asymmetry have not been studied by either of the groups.

In the present study, this asymmetry is seen to be the dominant cause of transfer of pulse energy towards longer wavelengths within the pulse (an effect usually attributed to intrapulse Raman scattering [42]). While the studies of Dudley et. al. and Nishizawa et. al. rely on cross-correlation FROG (or XFROG [41]), the study of Ogawa et. al. relies on two photon absorption FROG (or TPA FROG), and the study of Omenetto et. al. relies on a single shot SHG-FROG. The apparatus used in the present case is a highly simplified version of a single-shot FROG nicknamed GRENOUILLE (Grating Eliminated No-Nonsense Observation of Incident Laser Light E-fields) by its inventors, O'Shea et. al. [17]. Further, the results are presented in the form of a linear juxtaposition of the spectrogram (or short-time spectral history) [55] of the pulse with its optical spectrum, and its optical time-trace (similar to the nonlinear juxtaposition presented by Dudley et. al. [43]).

Section 2 discusses the experimental setup used and the method by which the experiment was carried out. Section 3 discusses the numerical model, and the results of the simulations that were carried out and compares the results with the experiment. Section 4 provides the conclusion.

4.2 Experimental Setup

Fig. 4.1 shows the experimental setup that is used (not drawn to scale). The experiments are done with polarized femtosecond pulses from a mode locked Ti:Sapphire laser (Spectra-Physics Tsunami) operating at a central wavelength of ~ 810 nm with a temporal pulse width (full width at half maximum or FWHM) of ~ 138 fs and a pulse repetition rate of 82 MHz. The laser light is coupled into a short ($\sim$6.9 cm)

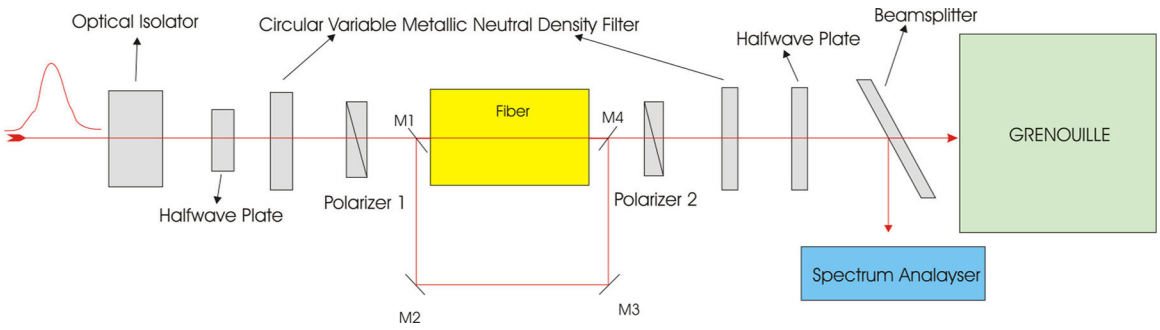

Figure 4.1: Block diagram of the experimental setup (not drawn to scale). The optical isolator prevents feedback into the mode-locked Ti:Sapphire laser from the input end of the fiber. The mirrors M1, M2, M3, M4 are placed only when measuring the FROG traces of the pulses input to the fiber. The input half-wave plate, polarizer 1 and polarizer 2 are used such that three possible configurations are studied - $\theta_{in} = \theta_{out} = \pm 45^o, 0^0$, where θ is the angle between the polarization of the input(output) light and the slow axis of the optical fiber. The output half-wave plate is used to rotate the axis of polarization of the output light to match with the axis of the nonlinear crystal in the GRENOUILLE setup. The optical spectrum analyzer is present as a cross-check for the FROG recovered pulses.

polarization maintaining optical fiber (Corning PM630, with a cutoff wavelength (wavelength above which the fiber can support a single transverse mode) of 630 nm, a core diameter of ~ 4 μm and a maximum beat-length of 2 mm - a method by which the beat length was measured accurately is given in the Appendix - section 4.5). A carefully aligned 10X microscope-objective and fiber holder (both mounted on together on an X-Y-Z micrometer translation stage) were used to achieve maximum coupling ($\sim$70%).

A Photon Inc. Beam Scan at the output end of the fiber is used to ensure that the coupled light has a single-transverse-mode (Multimode components could arise due to improper coupling and have to be carefully eliminated since the length of the fiber is extremely short). In order to achieve good coupling ($\sim$70%) without destroying the mode-locked condition of the Tsunami (which is unstable to feedback arising from reflection, primarily at the input end of the fiber), an optical isolator is placed immediately after the laser. The input power into the fiber is controlled using a metallic variable neutral density filter (VNDF). The combination of a half-wave-plate and a Glan Thompson linear polarizer is used to rotate the polarization of the pulses with respect to the fast and slow axes of the fiber. The polarizer is used to compensate for any leakage in the half-wave-plate.

Angles of input polarization of 0^o, and $\pm 45^o$ with respect to the fast(slow) axes are used. In the first case (0^o), we propagate pulses along one of the axes of the fiber. This case is chosen as it is easily amenable to modeling by a single nonlinear Schrödinger equation (generalized suitably to include the effects arising due to a sub-picosecond pulse width). In the second case, ($\pm 45^o$), the light intensity is equally

split along the two axes of the fiber. This is done in order to study the phenomenon of self-phase modulation (SPM) and degenerate-cross-phase modulation (DXPM) simultaneously for femtosecond pulses. In this case, interpulse walk-off between pulses traveling along the slow and the fast axes has to be taken into account when the simulations are performed, thus requiring a coupled set of two generalized nonlinear Schrödinger equations (one for each polarization component).

Measurements of the full electric field (intensity and phase) of the output pulses are performed using GRENOUILLE (Grating-Eliminated No-nonsense Observation of Ultrafast Incident Laser-Light E-fields), a highly simplified SHG-FROG device developed by O'Shea et. al. [17]. The GRENOUILLE-FROG setup used in our experiments is very similar to that developed by O'Shea et. al. [17]. Figure 4.2 presents the side view and some of the top view of the GRENOUILLE apparatus used.The cylindrical lens (to the left of the figure) focuses the incoming beam onto the crystal in one plane (i.e, the side view). In the other plane (i.e, in the top view), the Fresnel biprism (which has an apex angle of 168^o), splits the beam into two arms and causes the two arms to interact in a variable delayed fashion inside the crystal. In the zone where the two beams interact in the crystal in an overlapping fashion, the resulting second harmonic beam is the FROG beam. Since the SHG crystal acts like a grating, linearly varying output angle with output frequency, the FROG beam has a delay axis and a frequency axis. The spherico-cylindrical lens system collimates the diverging FROG beam in order for it to be captured appropriately by the CCD camera. The aperture before the camera is required to remove the component of the input beam that comes through the crystal without interacting with the opposite

arm, and which would otherwise saturate the camera and make the FROG beam invisible. The only difference between the GRENOUILLE displayed here and that documented by O'Shea et. al. [17] is that we use a spherico-cylindrical lens system in front of the CCD camera instead of a bi-cylindrical lens system similar to that used by O'Shea et. al. [17]. This departure is expected to result in a minor error in the linearity of the time-scale of the measured FROG traces, the error being largest for the diagonal elements trace.

The optical spectrum of the output pulses is also measured independently using an IST-REES E200 Series optical spectrum analyzer. This is done after the collimated fiber output beam is sent through a Glan Thompson polarizer (Polarizer 2 in Fig. 4.1), a neutral density filter, a half-wave plate and a beam splitter. The spectrum analyzer is used as a cross-check for the quality of the FROG recovered spectrum. Close agreement between the spectrum recovered using FROG and the one directly measured using the spectrum analyzer is found for the results presented here.

The axis of the output polarizer is chosen to be parallel to that of the input polarizer for all the three cases investigated (i.e. 0^o and $\pm 45^o$). For the $\pm 45^o$ case, the function of the output polarizer is to generate linearly polarized light by combining (interfering) the light that had propagated along both axes. For pulses traveling along one of the axes of the fiber (0^o case), the output polarizer would not be needed (in an ideal situation), since the pulses are linearly polarized upon exiting the fiber. We find it necessary to keep the output polarizer in the experiment in order to retain the beam alignment necessary for the GRENOUILLE and the Optical

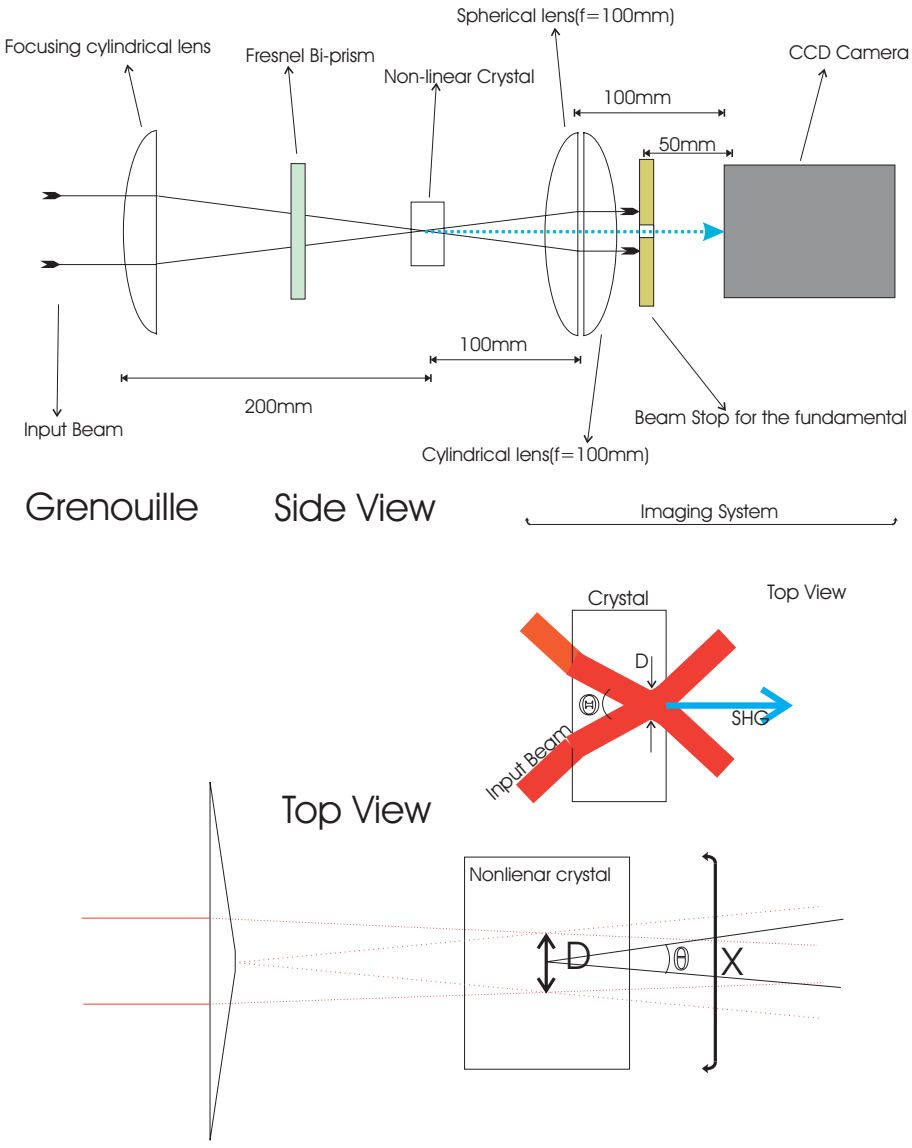

Figure 4.2: Schematic of the GRENOUILLE used, courtesy Silva, A.C. [56]

Spectrum Analyzer diagnostics while changing between the 0^o, $+45^o$ and the -45^o cases respectively.

The half-wave-plate after the filter is required in order to rotate the polarization of the light after the output polarizer until it is parallel to the axis of the nonlinear SHG crystal used in the GRENOUILLE apparatus. A 512 X 480 Pulnix TM CCD camera is used to photograph the SHG-FROG traces produced by the GRENOUILLE apparatus. A variable neutral density filter is used after the output half-wave-plate in order to prevent saturation of the CCD camera as this would result in distortion of the SHG-FROG trace generated. The FROG traces are recorded on a Dell Dimension desktop PC using a frame grabber. The FEMTOSOFT FROG-retrieval software is used to retrieve the electric field (both intensity and phase) of the pulses from the experimentally measured SHG-FROG traces, which have the following relationship with the electric field [41].

$$I_{FROG}(\omega,\tau) = |\int_{-\infty}^{+\infty} dt E(t)E(t-\tau)e^{i\omega\tau}|^2 \tag{4.1}$$

A brief and basic description of the FROG algorithm (see figure 4.3) is as follows -

We start with an initial guess of the complex electric field E(t)

1) Generate $E_{sig}(t,\tau) = E(t)E(t-\tau)$ (specific to SHG-FROG)

2) Fourier transform it to get $\tilde{E}_{sig}(\omega,\tau)$

3) Replace magnitudes of $\tilde{E}_{sig}(\omega,\tau)$ with those from $I_{FROG}(\omega,\tau)$, to get $\tilde{E'}_{sig}(\omega,\tau)$,

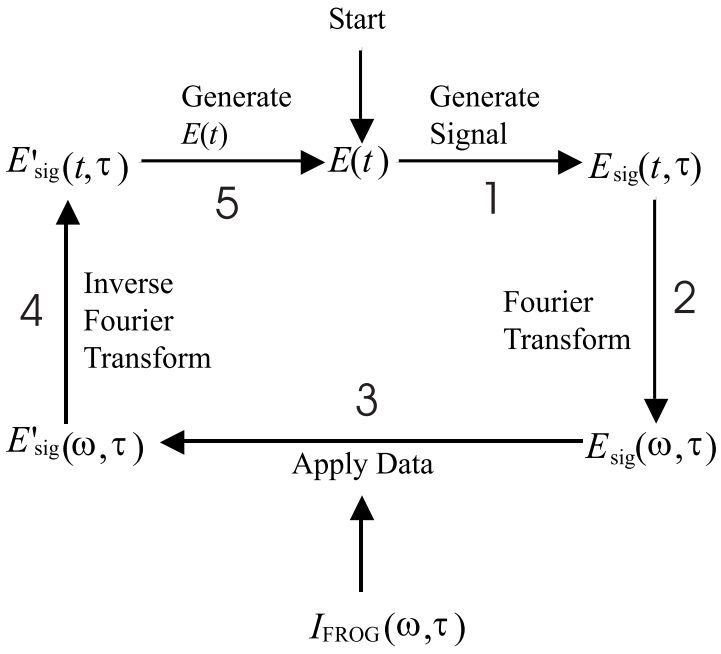

Figure 4.3: Schematic of a generic FROG algorithm, courtesy Trebino, R. [41]

in the following way -

$$\tilde{E'}_{sig}(\omega,\tau) = \frac{\tilde{E}_{sig}(\omega,\tau)}{|\tilde{E}_{sig}(\omega,\tau)|}\sqrt{I_{FROG}(\omega,\tau)} \tag{4.2}$$

4) Take the inverse Fourier transform of $\tilde{E'}_{sig}(\omega,\tau)$ to get $E'_{sig}(t,\tau) = E'(t)E'(t-\tau)$

5) Integrate $E'_{sig}(t,\tau) = E'(t)E'(t-\tau)$ over τ to get E(t)

Start over with step 1) until the until the results converge.

There are several improvements to this which make the FROG algorithm faster [41], but the basic structure of the algorithms used by FEMTOSOFT and other commercial software is the same.

We conducted experiments with power levels ranging from 50 mW to 790 mW of average (cw) power coupled into the optical fiber. The full electric field, however, was not recoverable for power levels $>$ 140 mW. Spectra and FROG traces were

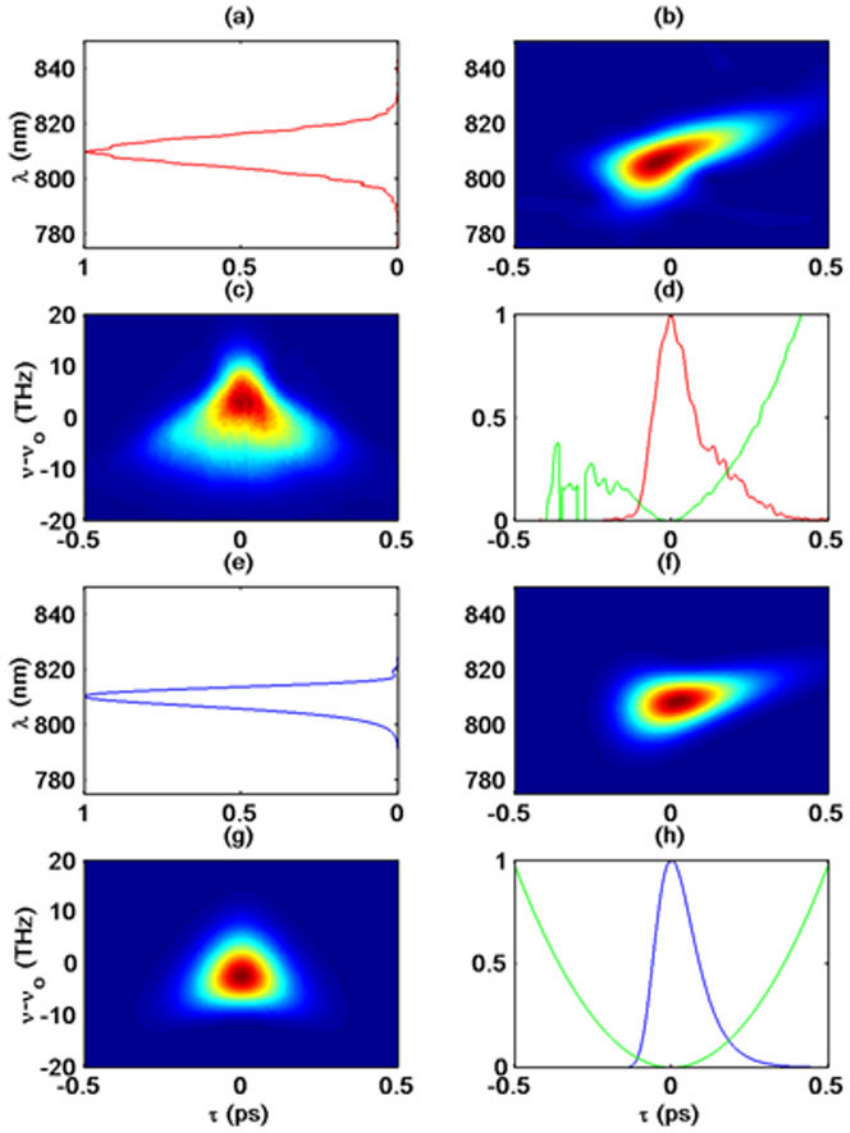

Figure 4.4: Input FROG traces (c & g), experiment (a-d) and simulation (e-h), juxtaposed with spectrograms (b & f), optical spectra (a & e) and optical time-traces (d & h).

measured for all the three combinations of input and output polarization angles considered. Qualitative agreement with simulations are found for all power levels.

In this work, we present results corresponding to a cw power of 140 mW (∼40 kW peak power, ∼6 nJ pulse energy) coupled into the fiber. The resolution of the SHG-FROG is 4.38 fs/pixel and 238 GHz/pixel respectively. The mirrors M1, M2, M3, M4 are placed only when measuring the FROG trace of the pulse input to the fiber. Care is taken to use metallic mirrors only, so that the polarization orientation of the pulses is not modified by the mirrors.

GRENOUILLE can accurately measure a pulse presenting a time-bandwidth product (TBP) of up to 10 [17, 56]. The input pulse satisfies these requirements quite well. However, the pulses output from the fiber have a pulse width of $\sim$ 1ps and a bandwidth of $\sim$ 40 THz implying a TBP of 40. Hence the comparisons between experiment and simulation are only qualitatively correct, as we stretched the GRENOUILLE to 4 times its maximum capability in terms of TBP.

GRENOUILLE was calibrated using 189 fs, 5.1 nm pulses with 0 chirp (TBP=1), converted into double pulses by passage through an etalon [56, 41]. Similar pulses were also used to accurately measure the beat-length of the fiber by recording the wavelength separation of the modulations produced after passage through 1 m of fiber. However, for our experiments we choose to work with an asymmetric (TBP $>$ 1) pulse configuration of 138 fs and 12 nm bandwidth. In the next section it will be shown that this input pulse asymmetry is instrumental in explaining the nature of the output spectra, which are found to have a transfer of pulse energy towards longer wavelengths.

4.3 Generalized CNLSE Model and Comparison with Experiment

All the simulations are done with the generalized NLSE using the split step Fourier method (SSFM) [42]. For the off-axis ($\theta = \pm 45^o$) simulations we are required to simulate two coupled equations, one for each polarization component of the propagating Electric field [42].

$$\frac{\partial A}{\partial Z} = i\gamma P_0 \left(|A|^2 A + \frac{2}{3}|B|^2 A - \frac{T_R}{T_0} A \frac{\partial |A|^2}{\partial \tau} \right) - \frac{i\beta^{(2)}}{2T_0^2}\frac{\partial^2 A}{\partial \tau^2} + \frac{\beta^{(3)}}{6T_0^3}\frac{\partial^3 A}{\partial \tau^3} - \frac{\alpha A}{2} \quad (4.3)$$

$$\frac{\partial B}{\partial Z} = i\gamma P_0 \left(|B|^2 B + \frac{2}{3}|A|^2 B - \frac{T_R}{T_0} B \frac{\partial |B|^2}{\partial \tau} \right) - \frac{d}{T_0}\frac{\partial B}{\partial \tau} - \frac{i\beta^{(2)}}{2T_0^2}\frac{\partial^2 B}{\partial \tau^2} + \frac{\beta^{(3)}}{6T_0^3}\frac{\partial^3 B}{\partial \tau^3} - \frac{\alpha B}{2} \quad (4.4)$$

A,B represent the normalized complex electric field envelopes of the two orthogonally polarized pulses traveling through the fiber along the fast axis and the slow axis respectively. Z is distance along the fiber in meters, τ is the normalized time measured in a frame of reference moving at the group velocity of the pulse along the slow axis [$\tau = (t - Z/v_{gs})/T_0$], where T_0 is the time-scale chosen for the simulations and is of the order of the pulse width ($\sim$ 138 fs FWHM). $\beta^{(2)} = 35$ ps^2/km is the group velocity dispersion coefficient, $\beta^{(3)} = 0.1$ ps^3/km is the third order dispersion coefficient, $\alpha \sim$6 dB/km = 0.0014 m^{-1} is the optical loss in the fiber material, and $\gamma = 0.019$ /Wm is the nonlinearity coefficient of the fiber for the central wavelength of 810 nm of the pulses [1]. P_0=40kW is the peak power of the input pulses corresponding to a cw power of 140 mW and a pulse energy of 5.5

nJ. d $\sim$ 2.2 ps/m is the polarization mode dispersion coefficient or pulse walk-off parameter which governs the rate of walk off between the two orthogonally polarized pulses propagating along the two axes of the fiber and can be calculated from the experimentally estimated beat-length (described later in this section). T_R ($\sim$ 3 fs) [42] represents the slope of the Raman-gain function for the operating frequency.

The following length scales give an idea of the processes involved and their relative importance in the dynamical evolution of the pulse along the fiber length :-

$$\begin{aligned} L_{NL} &= \frac{1}{\gamma P_0} \sim 1.3mm \\ L_w &= \frac{T_0}{d} \sim 6.3cm \\ L_{D_2} &= \frac{T_0^2}{\beta^{(2)}} \sim 54cm \\ L_{D_3} &= \frac{T_0^3}{\beta^{(3)}} \sim 26m \\ L_{IRS} &= \frac{T_0}{T_R} L_{NL} \sim 6cm \\ L_\alpha &= \frac{1}{\alpha} \sim 700m \end{aligned} \tag{4.5}$$

"NL" stands for nonlinear, "w" for linear pulse walk-off arising due the difference in group velocities between the slow and the fast axes, "D_2" and "D_3" stand for 2nd and 3rd order dispersion respectively, "IRS" stands for intrapulse Raman scattering, and "α" stands for fiber loss [42].

Looking at the length scales, it may appear that ignoring the IRS and 2nd order dispersion terms, an analytical solution may be possible. It should be noted however, that the linear walk-off term is still present and does not commute with the nonlinear terms in a Split-Step Fourier Method (SSFM) formalism. This enforces the

requirement of small ($\sim$ 1 mm) step-size of integration unlike the analytic solution which is equivalent to an SSFM implementation with a step-size equal to the length of the fiber (6.9 cm).

The nonlinear length is the smallest, much smaller than the fiber length, indicating that nonlinearity played a dominant role. The linear walk-off length is comparable to the fiber length indicating that its effect is considerably less important. The group velocity dispersion length, is larger than the fiber length by a factor of 8, and it is expected that dispersion effects are largely absent. Since we are interfering pulses that are propagating along both axes of the fiber, the small effects of linear walk-off and group velocity dispersion are greatly increased giving maximum interference at the 45^o angle. L_{IRS} is of the order of the fiber length and the above comparison of length scales indicates that IRS should be of little importance in the dynamics. This is observed to be the case with the numerical results. All the asymmetry in the output pulse, which is generally attributed to IRS, is found to be primarily due to the asymmetry of the input pulse. The asymmetry of the input pulse plays an important role in its spectral evolution. The input pulse had a leading edge, as seen in fig. 4.4(d), and causes (as a result of the simulations), a transfer of pulse energy towards longer wavelengths. This is an effect similar to the self-frequency shift caused by IRS. Simulations carried out ignoring IRS but including pulse asymmetry give the same results as the simulations including both IRS and pulse asymmetry. Conversely, simulations carried out including IRS but ignoring pulse asymmetry give too weak a transfer of pulse energy towards longer wavelengths compared to the experiments. The modulation lobes visible in the ex-

perimental optical spectra for the $\pm 45^o$ cases are very weak or even absent in this case. For these reasons, we conclude that IRS does not play an important role in the dynamics, although it is likely to gain importance for longer fiber.

The equations are integrated using the split-step Fourier method (SSFM) [8], a step size $\Delta Z = 0.1$ mm is found to be sufficiently small for convergent results. The method assumes the slowly varying envelope approximation which is a good approximation in the present case.

The SHG-FROG trace is a special form of the spectrogram or short-time spectral history [55]

$$S(\omega, \tau) = |\int_{-\infty}^{+\infty} dt E(t) g(t-\tau) e^{-i\omega\tau}|^2 \tag{4.6}$$

where g(t-τ) is a variable-delay gate function [41]. g(t-τ) = E(t-τ) is a natural choice of the gate function for the experiment (i.e. gating the Electric field of the pulse with itself, since only the optical pulse itself, has a time-scale small enough to be comparable to its own femtosecond time-scale) [41]. The time-trace and the optical spectrum of the input and output pulses can be computed from the SHG-FROG trace using the FEMTOSOFT FROG algorithm software. The SHG-FROG representation however, is not the most intuitive for comparison with the recovered time-trace and spectrum. No linear, one-to-one correspondence is seen between features in the SHG-FROG trace and features in the time-trace and optical spectra upon juxtaposition. Moreover, it is difficult to discern the temporal evolution of the spectral content of the pulse from its leading edge to its trailing edge by looking at

the SHG-FROG trace. In this sense, the SHG-FROG trace is not the most intuitive representation of the time-wavelength structure of the pulse. A time-wavelength spectrogram or short-time spectral history is computed from the recovered Electric field time-trace using the gate function given below -

$$g(t-\tau) = exp - \frac{(t-\tau)^2}{2t_{win}^2} \tag{4.7}$$

t_{win} is the size of the window-width chosen for the Gaussian gate. It is important to choose t_{win} to be smaller than the temporal extent of the output pulses. However, care must be taken to keep t_{win} large enough to have a good wavelength resolution in the spectrogram. The value chosen in the present case is $t_{win} = 0.2$ ps (FWHM) which is smaller than the temporal extent of the output pulses (~ 1.5 ps) but larger than the input pulse (0.138 ps FWHM). Effects of varying the size of the window can be seen in figure 4.5. Figure 4.5 (a) to 4.5 (h) represent experimental spectrograms for the $+45^o$ case computed with gate sizes varying from 8.76 femtoseconds to 1.138 ps full-width at half maximum (FWHM). Clearly, choices (e) and (f) give the best combination of time and wavelength resolution. The window-width that is found to be optimum is 0.2 ps FWHM and is used consistently throughout the results presented here. The significance of the particular nature of the $+45^o$ spectrogram is discussed later in this section and is also depicted in figure 4.7. This is an invertible representation [55] and the SHG-FROG trace can be recovered from it with knowledge of the gate function.

Figure 4.4 shows experimental and simulated versions of the input pulse, its

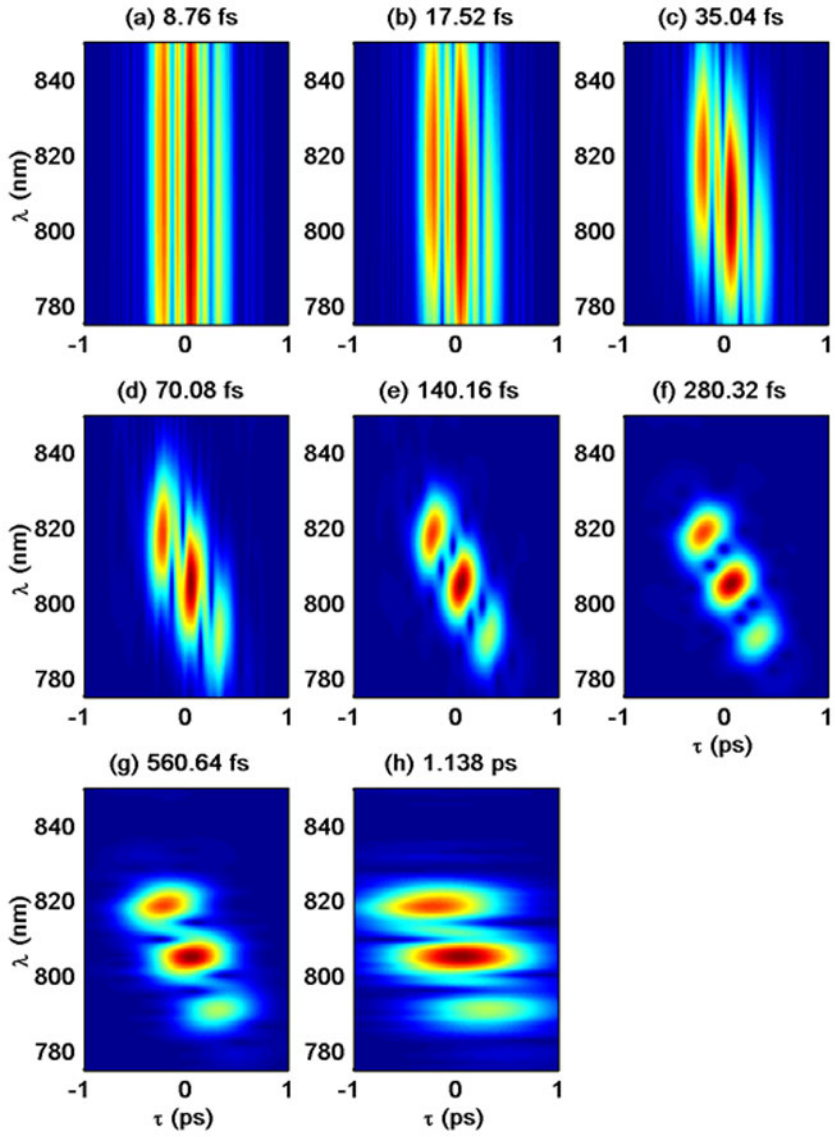

Figure 4.5: Changes in the experimental spectrogram as a result of changes in the width of the Gaussian gate function. The optimal gate width is found to be 0.2 ps, in between choices (e) and (f) which appear in this figure to give the best temporal and spectral resolution.

time-trace, spectrogram, optical spectrum and FROG trace juxtaposed in such a way that it visually possible to correlate corresponding features such as peaks and troughs between the spectrogram, the optical spectrum and the time-trace. Such a juxtaposition is not possible with the SHG-FROG traces. Such a juxtaposition is also presented by Dudley et. al. [43] with an XFROG trace serving as a spectrogram. The deficiency of their juxtaposition is that the wavelength scale of the optical spectrum has to be stretched nonlinearly for an accurate comparison. Figure 4.4(c) represents the measured SHG-FROG trace. Figures 4.4(a) and 4.4(d) represent the input optical spectrum and optical time-trace recovered from the FROG trace shown in 4.4(c) using the FEMTOSOFT FROG software. Figure 4.4(b) represents the experimental input spectrogram computed from the FROG trace in figure 4.4(c). Figures 4.4(e)-4.4(h) represent the corresponding input pulse characteristics of the assumed input pulse for the simulations. The green curve in both 4.4(d) and 4.4(h) represents the phase distribution with time. Note the asymmetry in the experimentally measured input time-trace (4.4(d), intensity (red-curve), and phase (green curve)), which is reproduced to a certain extent in the input pulse used for the simulations (4.4(h), intensity (blue-curve)). The input pulse is assumed to be linearly chirped (hence the parabolic phase distribution (green curve in 4.4(h))).

Figures 4.6, 4.7 and 4.8 give similar juxtapositions for the output pulses, for the θ=-45^o, +45^o and 0^o respectively. In all three cases a clear shift of pulse energy towards longer wavelengths, accompanied by considerable spectral and temporal broadening can be seen. This is attributable to the effects of SPM and DXPM with the effects of SPM being stronger (due to the 2/3 factor in Eqs. 1 and 2). Moreover,

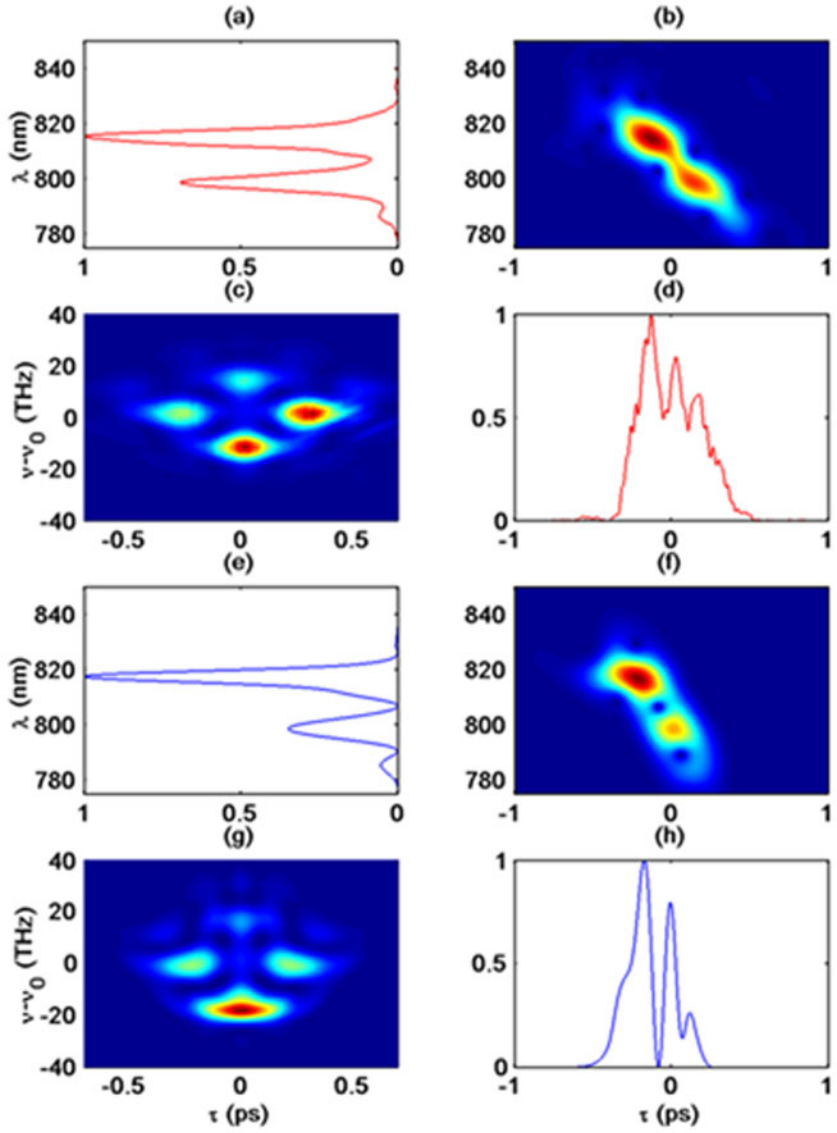

Figure 4.6: Experimental (a-d) and Simulated (e-h) t-λ spectrograms (b & f) for $\theta = -45^o$ juxtaposed with corresponding time-trace (d & h), optical spectrum (a & e) and SHG-FROG trace (c & g).

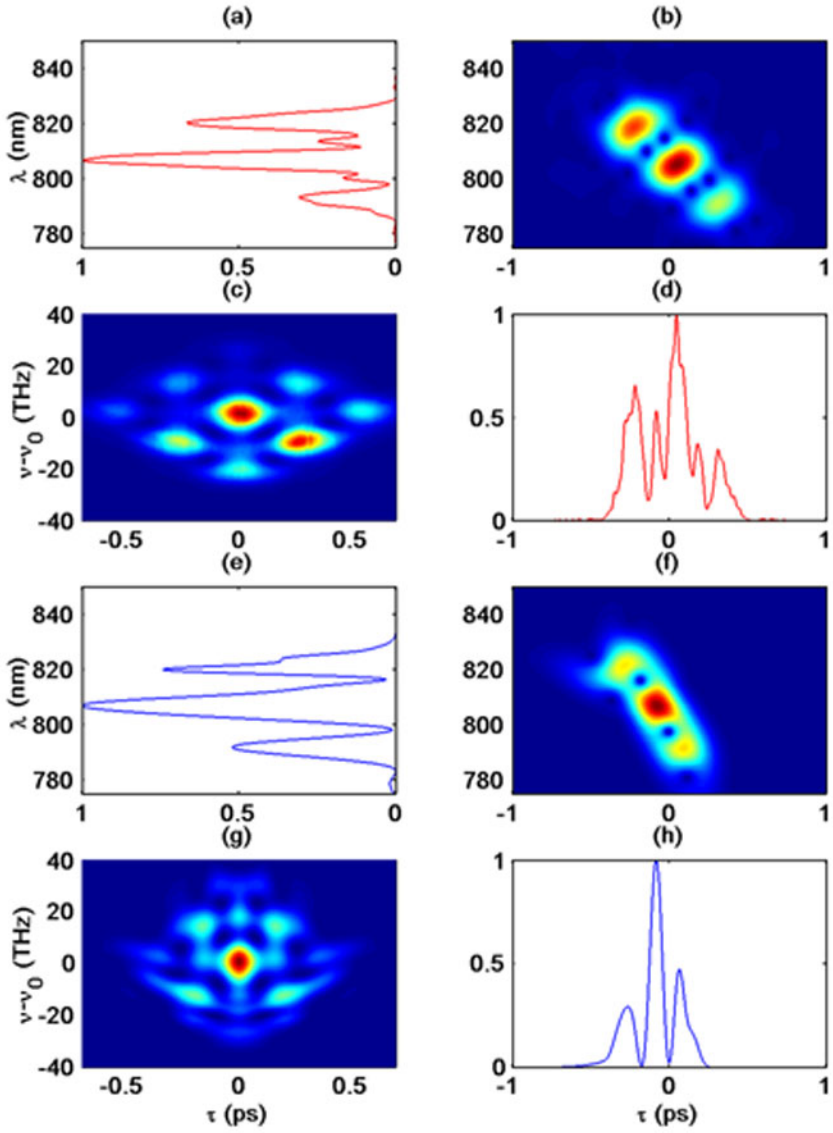

Figure 4.7: Experimental (a-d) and Simulated (e-h) t-λ spectrograms (b & f) for $\theta = +45^o$ juxtaposed with corresponding time-trace (d & h), optical spectrum (a & e) and SHG-FROG trace (c & g).

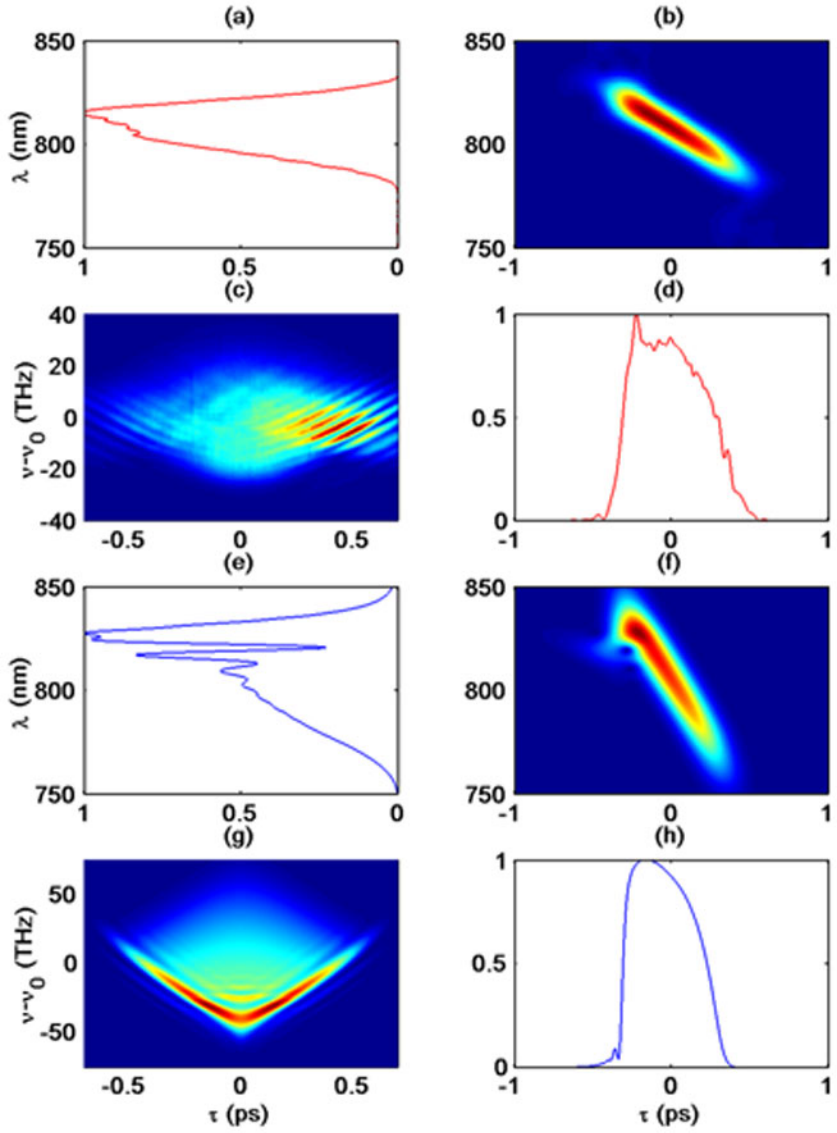

Figure 4.8: Experimental (a-d) and Simulated (e-h) t-λ spectrograms (b & f) for $\theta = 0^o$ juxtaposed with corresponding time-trace (d & h), optical spectrum (a & e) and SHG-FROG trace (c & g).

the strong asymmetrical spectral broadening observed, can be easily explained by SPM effects alone. If the initial optical pulse presents a strong temporal asymmetry with a steep leading edge, SPM will generate more Stokes frequencies than snti-Stokes frequencies, thus resulting in an overall red-shift. In figures 4.6 and 4.7 the temporal and spectral modulations seen arise from interference between the two output polarization components of the pulse that are coherently combined by the output polarizer. These modulations are due to pulse walk-off or polarization mode dispersion. Figure 4.9 gives a comparison between a simulation in which DXPM was neglected altogether (blue curves) and one in which it was included (red curves). Clearly, the effects of DXPM are limited to spectral and temporal broadening, and its contribution towards the asymmetry is minimal.

The simulations were found to be very sensitive to the exact nature of the input pulse. That is, the intensity and phase of the numerically assumed input pulse has to be as close as possible to that of the actual input pulse coupled into the fiber in the experiments. The experimentally measured input trace used in this work is shown in Fig. 4.4 along with its corresponding optical spectrogram juxtaposed with the recovered time-trace and optical-spectrum. The input pulse assumed for the simulations was a pulse analytically fitted to the experimental input pulse with the following asymmetric analytic function -

$$U_x(t,0) = \exp\left[1 + \tau - \exp(-\tau) + ic\tau^2\right] \tag{4.8}$$

which can also be expressed as -

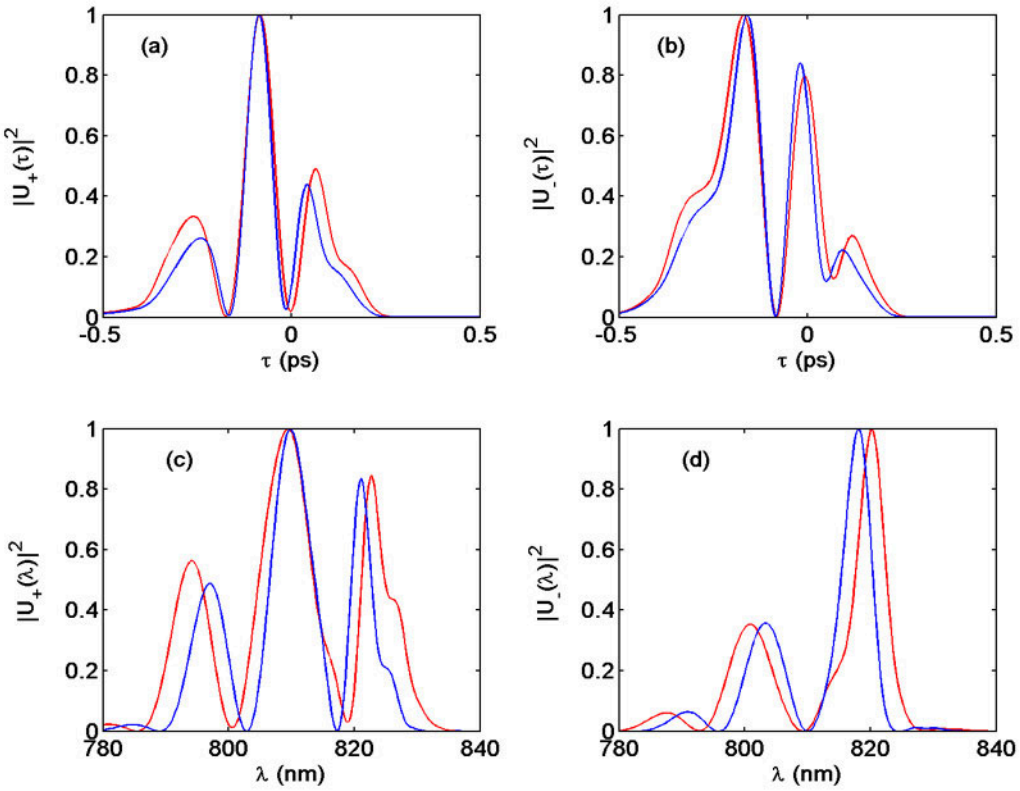

Figure 4.9: Comparison between simulations neglecting DXPM (blue curves) and those including DXPM (red curves). (a) and (b) Time-traces for the θ=+/-45^o cases, (c) and (d) Optical spectra for the θ=+/-45^o cases

$$U_x(t,0) = \exp\left[-\frac{\tau^2}{2}\left(1 - ic - \frac{\tau}{3} + \frac{\tau^2}{12} - \frac{\tau^3}{60} + ...\right)\right] \tag{4.9}$$

where $\tau = t/T_0$, $T_0 \sim 86$ fs and c $\sim$ -0.32 are the 2 parameters used in defining the analytic function. The values of these 2 parameters are found by nonlinear least square fitting.

The phase profile of the chosen analytical pulse does not exactly reproduce the phase profile of the experimental pulse. The reason for this (as can be seen in Figure 4.10) is that the phase profile was observed to fluctuate from pulse to pulse. Moreover, for the times when the intensity was non-zero, the average phase was well approximated by a quadratic function of time. This is te reason for selecting a quadratic (linearly chirped) phase profile for the input pulse.

In all the output experimental FROG traces, i.e. figs. 4.6(c), 4.7(c), and 4.8(c), the mirror reflection symmetry characteristic of SHG-FROG traces is seen to be absent. This is possibly due to pulse-front tilt [60]. This is partially taken into account by the FEMTOSOFT FROG algorithm which "knows" that the traces are SHG-FROG traces [41]. Since the results are qualitative, this is a minor discrepancy. Looking at the $\pm 45^o$ cases, it is observed that both the experimental and simulated spectrograms have the same number of lobes. This feature is also seen in the optical spectra and to a certain extent in the optical time trace too. The bandwidths and pulsewidths of the simulated and experimental pulses is observed to be similar. The spectrogram representation is well suited for simultaneous comparison with both the optical spectrum and the optical time-trace (red curves - experimental, blue curves

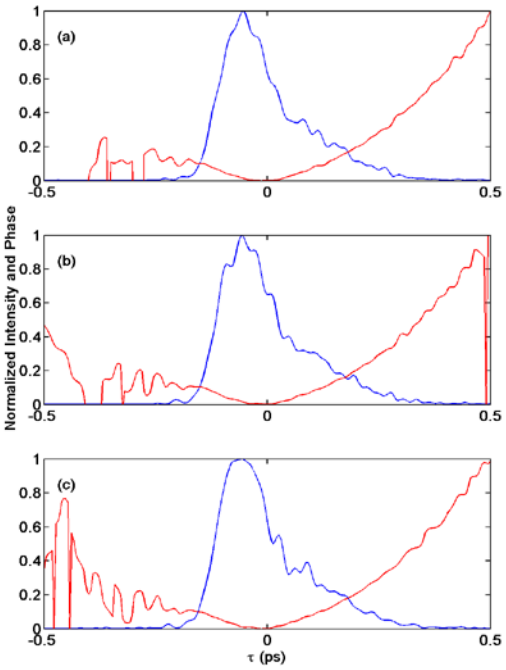

Figure 4.10: Variations in phase profiles of the input pulse for 3 different measurements (a)-(c). The phase profile is best approximated by a quadratic function of time over the region where the intensity is non-zero

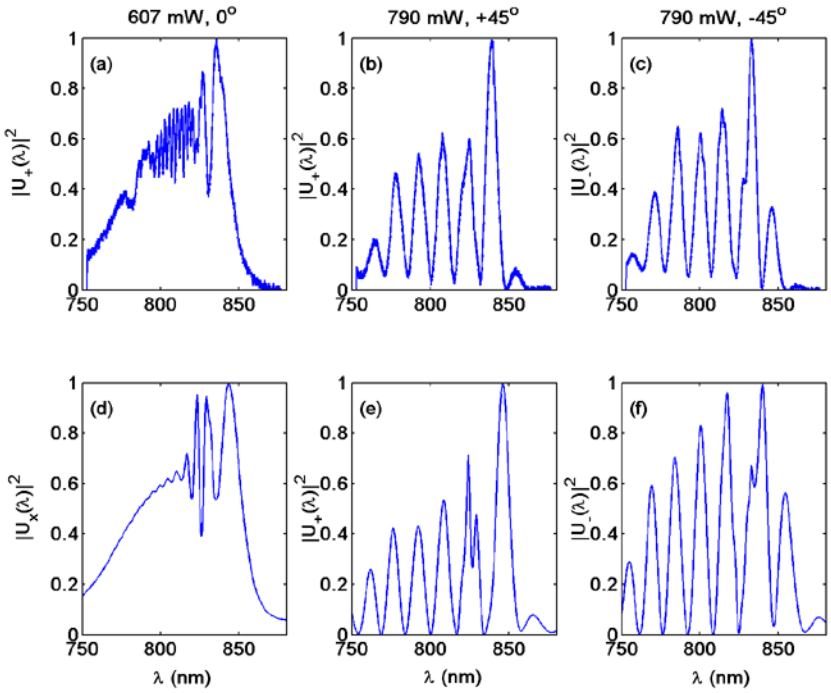

Figure 4.11: Comparison between experimental (top row) and simulated (bottom row) optical spectra showing good qualitative agreement. Note, power levels are much higher than the 140 mW case considered earlier

- simulation). The optical spectrum and the optical time-trace can be viewed as orthographic projections of the spectrogram. Good qualitative agreement is seen between simulations and experiment.

The agreement does not restrict itself to the 140 mW case but is also observed for all measured powers. The difference being (as pointed out earlier), the full electric field was not recoverable for powers greater than 140 mW. In figures 4.11 and 4.12, experimental and simulated comparisons of the optical spectra, and FROG traces for cw coupled powers of 790 mW ($\pm 45^o$) and 607 mW (0^o) are presented. The spectra

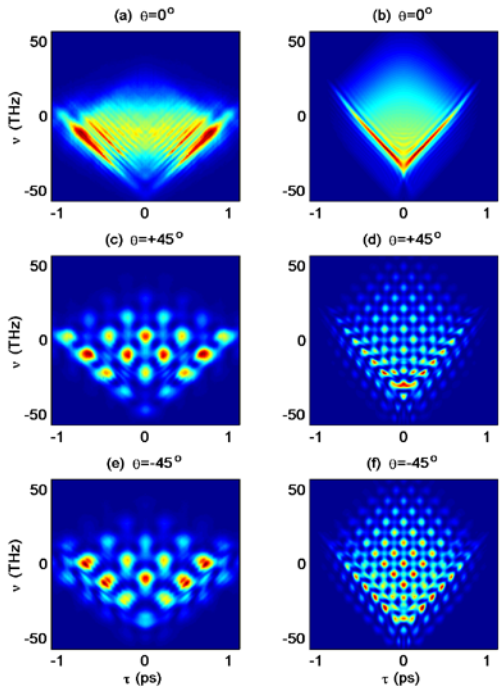

Figure 4.12: Comparison between experimental (left column) and simulated (right column) FROG traces. (a) and (b) correspond to 0^o and 607 mW; (c) and (d) correspond to $+45^o$ and 790 mW; (e) and (f) correspond to -45^o and 790 mW. The experimental FROG traces have a lower resolution compared to the simulations, partially explaining the discrepancy.

agree very well, and the experimental FROG traces agree upto the limits of frequency resolution of the nonlinear crystal. Figs. 4.11(a) and 4.11(d) show comparisons of the experimental and simulated optical spectra for the 0^o case. Figs. 4.11(b) and 4.11(e) show the corresponding comparisons for the $+45^o$ case, and figs. 4.11(c) and 4.11(f) show the comparison for the -45^o case. Fig. 4.12 compares the experimental and simulated FROG traces for these high coupled power cases mentioned earlier in this paragraph. Figs. 4.12(a) and (b) represent the 0^o case, figs 4.12(c) and (d) represent the $+45^o$ case, and figs. 4.12 (e) and (f) represent the -45^o case. The outlines of the FROG traces agree very well, but the inner details don't agree so well. This may be because for such high powers, the FROG traces develop intricate structures that are not resolvable by the crystal's finite resolution. It is possible that with knowledge of the crystal's frequency resolution, one could convolve the simulated FROG traces and hence achieve better agreement with the experimental FROG traces. For the experimental FROG traces presented in fig. 4.12, in order to make better comparisons with simulation, the pulse-front tilt mentioned earlier, has been balanced by imposing mirror reflection symmetry about the τ=0 ps axis. For these higher powers ($\sim$ 5 times larger compared to 140 mW), the nonlinear length scale (L_{NL}) and the length scale associated with intrapulse Raman scattering (L_{IRS}) are a factor of 5 smaller. The effects of IRS are still found to be negligible compared to the effects of SPM, even though L_{IRS} is now smaller than the fiber length by a factor of 5. This is expected as the as L_{NL} is still much smaller than L_{IRS}, by the same factor as before (both length scales depend inversely on the pump power).

At this point it is worth pointing out and discussing the method in which the

experimental beat length and walk-off parameter were calculated and the physics that underlies this procedure. It so happens that the method is also closely related to one of the potential applications of this experiment. The derivation of the relation between the modulation spacing and beat-length (and the walk-off parameter) is as follows :-

It is sufficient to consider only the linear part of the CNLSEs, in fact even among the linear terms, it suffices to consider only the first order term and ignore the higher order dispersion terms. The CNLSEs then take the form :-

$$\begin{aligned} \frac{\partial A}{\partial Z} &= 0 \\ \frac{\partial B}{\partial Z} + \frac{d}{T_0}\frac{\partial B}{\partial \tau} &= 0 \end{aligned} \tag{4.10}$$

The input wave functions of the electric field polarizations are assumed to be linearly chirped Gaussians of the following form :-

$$\begin{aligned} A(\tau,0) = B(\tau,0) &= exp\left[-(1+iC)\frac{\tau^2}{2}\right] \\ \tilde{\mathrm{A}}(\omega,0) = \tilde{\mathrm{B}}(\omega,0) &= \left[\frac{2\pi}{1+iC}\right]^{\frac{1}{2}} exp\left[-\frac{\omega^2}{2(1+iC)}\right] \end{aligned} \tag{4.11}$$

They are propagated along the fiber length using the SSFM as follows :-

$$A(\tau,z) = A(\tau,0)$$

$$\tilde{\mathrm{A}}(\omega,z) = \tilde{\mathrm{A}}(\omega,0)$$

$$\tilde{\mathrm{B}}(\omega, z) = \tilde{\mathrm{B}}(\omega, 0) exp(-i\omega dz) \tag{4.12}$$

Here $\tilde{\mathrm{B}}$ denotes the Fourier transform of B.

C is the polarization component at 45^o to the axes of the fiber and propagates as follows :-

$$\tilde{\mathrm{C}}(\omega, z) = \frac{\tilde{\mathrm{A}}(\omega, z) + \tilde{\mathrm{B}}(\omega, z)}{\sqrt{2}} = \tilde{\mathrm{B}}(\omega, 0) exp\left(-\frac{i\omega dz}{2}\right) cos\left(\frac{\omega dz}{2}\right)$$
$$|\tilde{\mathrm{C}}(\omega, z)|^2 \propto cos^2\left(\frac{\omega dz}{2}\right) \propto cos^2\left(\frac{\pi c dz}{\lambda}\right) \tag{4.13}$$

Since $\cos^2(\theta)$ is periodic with $\Delta\theta = 2\pi$ this implies that the frequency spacing of the modulations is given by :-

$$\Delta\omega dz = 2\pi \tag{4.14}$$

The walk-off parameter d, is related to the beat length B, by -

$$d = \frac{\lambda_0}{Bc} \tag{4.15}$$

$$\Delta\omega = \frac{2\pi B}{\lambda_0 z} \tag{4.16}$$

The frequency of the nth modulation peak (or trough, depending on whether we choose $+45^o$ or -45^o is given by -

$$\omega_n = \omega_0 + n\Delta\omega = \omega_0 \left[1 + \frac{nB}{z}\right] \tag{4.17}$$

This further implies that the wavelength of the nth modulation peak/trough is given by -

$$\lambda_n = \lambda_0 - n\Delta\lambda = \frac{\lambda_0}{1 + \frac{nB}{z}} \tag{4.18}$$

The relationship between the wavelength separation $\Delta\lambda$ and the beat length B can be found by using a power series expansion of the above expression and is given by -

$$\Delta\lambda_n \sim \frac{\lambda_0 nB}{z}, \text{ when } \frac{nB}{z} \ll 1 \Rightarrow B \sim \frac{\Delta\lambda z}{\lambda_0} \tag{4.19}$$

It was found that for a 1 meter length of fiber, and 810 nm input pulse central wavelength, the wavelength spacing of the modulations at the output was $\sim$ 1 nm implying a beat length of $\sim$ 1.2 mm. The relationship between the beat length and the walk-off parameter (Eqn. 4.12) implies that the a walk-off parameter of $\sim$ 2.2 ps/m.

Figure 4.13 shows the simulated FROG trace, spectrogram, time trace, and both the simulated and experimental optical spectra for a 1 meter long fiber for an input pump power of the order of 100 mW (cw). The input pulses were symmetric and had an FWHM of 180 fs, with a chirp of $\sim$ 2. The CNLSE approach described earlier was used for the simulations. The time-trace is not centered around o ps because the time τ is measured in a frame of reference moving at the group velocity of the slow axis of the fiber. Pulses traveling at θ=+45^o lead the slow axis, therefore the pulse is centered on a time greater than 0 ps. The time-bandwidth

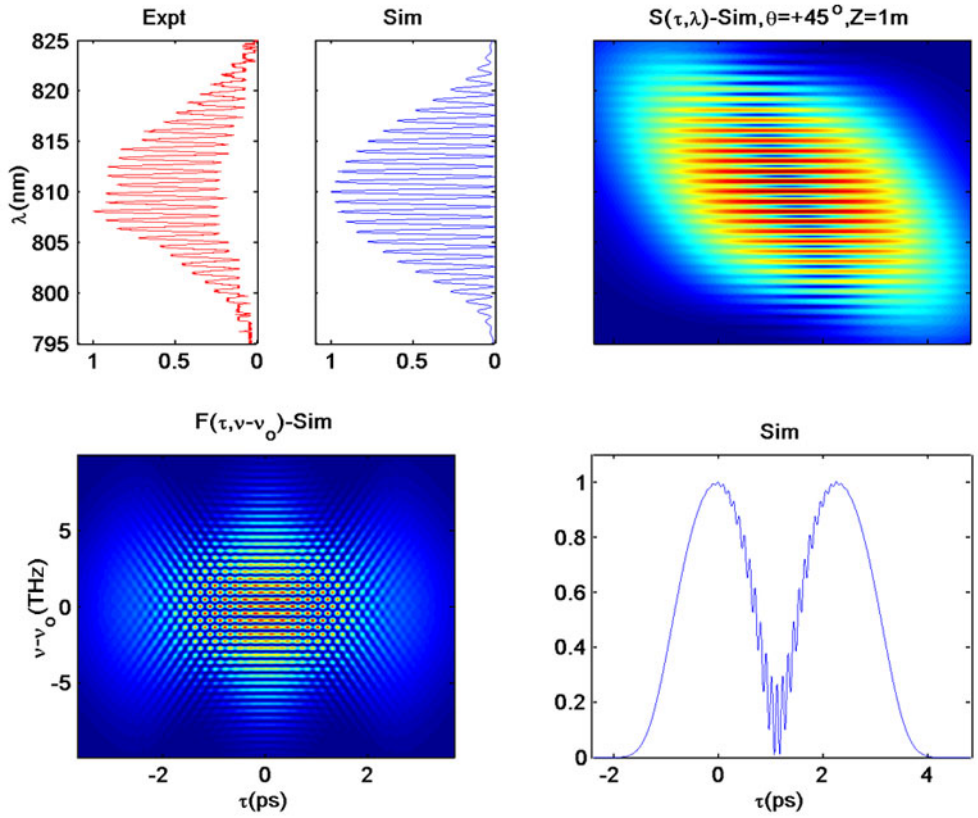

Figure 4.13: Simulation results accompanied by experimental optical spectrum for 180 fs pulses propagating through and optical fiber. Fig(a) shows the experimental optical spectrum, Fig(b) shows the simulated optical spectrum, Fig(c) the simulated spectrogram, Fig(d) the simulated SHG-FROG trace and fig(e) the simulated time trace. The evenly spaced modulation spectra indicate possible applications towards wavelength division multiplexing (WDM)

product (TBP) of the output pulses was too large ($\sim$ 80)for it to be captured by the GRENOUILLE FROG apparatus. The evenly spaced nature of the modulations and the broadband nature of the envelope of the spectra indicates a possible application towards producing evenly spaced wavelength sources for a wavelength division multiplexing (WDM) setup. It is a flexible source as the number of modulations can be increased by increasing the pump power, the modulation spacing can be varied by varying the fiber length (longer fiber providing closer spacing).

4.4 Conclusion

We have measured and characterized nonlinear modulation (SPM and DXPM) of asymmetric femtosecond pulses propagating through a short birefringent single mode fiber both experimentally and numerically. We observe good qualitative agreement between GRENOUILLE based experiments and CNLSE based simulations. We present the results using a linear spectrogram (short time spectral history) function of a pulse which is then juxtaposed with its optical spectrum and time-trace for easy visual comparison. It is observed that the output pulses are highly asymmetric towards longer wavelengths; this asymmetry is determined to be caused by asymmetry in the input pulse's temporal profile and not by IRS governed self-frequency shift. We have measured pulses having a TBP of 40, well over the advisable limit of 10 [17, 56] for GRENOUILLE. Recent improvements in the maximum measurable bandwidth of GRENOUILLE [58, 59] may help in making the present and similar results more quantitative. The results of this investigation indicate that a possible practical application would be to modulate short pulses, both temporally and spec-

trally, by passage through such polarization maintaining optical fibers with specified orientation and length.

Chapter 5

Conclusion

In this thesis the propagation of light pulses through an optical fiber (in the nonlinear regime) has been investigated. This research consists of experimental, theoretical and numerical computations. The focus of this work has been to experimentally record pulsed laser beam characteristics before and after a given optical fiber, and, to try and understand the underlying dynamics by performing numerical simulations based on realistic theoretical models. The nonlinear phenomena studied include multiple four-wave-mixing processes, stimulated and intrapulse Raman scattering, self-phase modulation and cross-phase modulation. This chapter provides a summary of the various achievements in the study of the aforementioned nonlinear processes, which have been discussed in detail in the previous chapters.

5.1 Four-wave-mixing

Chapter 2 reports the results of a numerical study of the dynamical evolution of four-wave-mixing (FWM) processes in a single mode optical fiber when broadband multiplicative phase noise is taken into account. The origin of the phase noise is traced to fluctuations in the linear refractive index of the fiber. This in turn is shown

to provide a means by which the evolution of FWM processes along a fiber can be used to probe inhomogeneities (temperature and density fluctuations) in the fiber core, since the inhomogeneities produce fluctuations in the linear refractive index.

A theoretical model is developed wherein the nonlinear Schrodinger equation (NLSE) is augmented with linear multiplicative noise. The split-step Fourier method (SSFM) used to numerically solve the modified NLSE is described with emphasis on the method in which the phase noise is incorporated. The simulations are carried out with much higher frequency resolution (60 MHz), frequency span (16 THz) and time bandwidth product (TBP $\sim$ 2500) compared to previous studies based on a truncated coupled ODE model [28], without sacrificing on computational efficiency.

The importance of incorporating the physical features unique to the pump lasers into the model is demonstrated. It is shown that incorporation of the fact that one of the pump lasers was bichromatic with two very closely spaced longitudinal modes, gave much better results than the assumption that they were both monochromatic. The two longitudinal modes were spaced by 0.5 GHz as compared to the detuning of 366 GHz, an effect of 1 part in 700. Incorporation of the fact that the laser light was pulsed, with a 5 ns pulse width, is shown to give better results than cw simulations. These points are elucidated through graphical comparisons of the experimental and simulated evolutions of the 1st and 2nd order sidebands generated through FWM.

Two kinds of stochasticity enter the simulations. The fluctuation in the power level of the pump lasers and the linear multiplicative phase noise due to refractive index fluctuations are both shown to be important in explaining the dynamics.

The power fluctuations ranged from 5% - 20%. The refractive index fluctuations were of the order of $\sigma_n^2 \sim 10^{-17} m^{-1}$, translating to a fiber core density variation of $\Delta\rho/\rho \sim 10^{-6}$ or 1 part per million. Thus the experiment can be used as a sensitive probe of fiber medium inhomogeneities.

Detailed comparisons are made with the experimental results of Hart et. al. [28] and the agreement is excellent.

5.2 Raman Scattering

In Chapter 3, efficient numerical algorithms for the simulation of stimulated Raman amplification, spontaneous Raman generation and intrapulse Raman scattering, along an optical fiber are developed and executed. This is done since Raman processes were postulated to be one of the physical sources of stochastic phase fluctuations in the dynamical evolution of four-wave-mixing processes discussed in chapter 2. Algorithms utilizing inherent conservation laws of the governing coupled nonlinear Schrodinger equations (CNLSEs) are implemented into the split-step Fourier method (SSFM).

At first, a model involving a Stokes seed pulse with no spontaneous Raman generation is considered. The model is bench marked with results available in the literature [27]. The seed is chosen to consist of noise with a spectrum similar to the Raman gain spectrum. The total power contained in the seed is chosen to be much smaller than the pump power (by three orders of magnitude), consistent with the experiments reported by Hart et. al. [28], where no Stokes wave was observed. The results of the simulations carried out with this model show a Stokes pulse generating

from broadband noise and subsequently walking-off with respect to the pump pulse. The results also clearly indicate that the amplification of the Stokes wave has a negligible effect on the evolution of the sidebands for fiber lengths < 50 meters, but considerable sideband depletion is observed for fiber lengths ranging from 50 meters - 150 meters.

The model referred to above did not have the feature of a Raman pulse spontaneously and stochastically generating from zero initial conditions. A seed pulse was necessary, and all the stochasticity was due to the particular choice of a noisy seed pulse. Stochasticity is inherent to Raman scattering and a model that incorporated this in a physical way was found in order to achieve this [37]. The inclusion of phase noise effects due to Raman generation and Raman amplification was carried out suitably by deriving and implementing an algorithm to solve the new set of stochastic CNLSEs. It was found that while the Raman processes did lead to stochastic phase fluctuations, these fluctuations were too weak to have any noticeable effect for the pump powers and fiber lengths of interest in the four-wave-mixing study discussed in chapter 2. However, for larger powers, and longer fibers it was found that energy of the Stokes wave grows stochastically, although monotonically, while stochastically and monotonically depleting the pump wave.

The process of intrapulse Raman scattering which involves transfer of pulse energy from shorter wavelengths to longer wavelengths was also studied numerically. An algorithm to suitably include it into the split-step Fourier method was developed. The implications of this effect too were found to be negligible for the parameters of the four-wave-mixing experiment, although its significance grew for larger powers

and longer fibers.

5.3 Ultra-short Pulse Propagation

Chapter 3 presents an experimental and computational study of self- and cross-phase modulation of femtosecond pulses propagating through a polarization-maintaining optical fiber. The experiments are carried out using the novel GRENOUILLE technique [17] which enables one to obtain the intensity, phase and spectrum of the electric field of the incident light. The beam propagation experimental setup and the GRENOUILLE apparatus are described in detail. GRENOUILLE traces of both, the light incident on the fiber and the light emergent from the fiber are recorded. The emergent traces and recovered electric fields are compared with results from numerical simulations carried out with a coupled nonlinear Schrodinger equation (CNLSE) model based on the split-step Fourier method (SSFM). It is revealed by this study that the spectral asymmetry that is observed in the output pulses is directly related to the temporal asymmetry of the input pulses, and not to other effects such as Raman induced self-frequency-shift. Experimental data are taken for peak coupled power levels ranging from 40 kW (140 mW cw) to 230 kW (790 mW cw), and good qualitative agreement between experiment and simulation is observed. A linear spectrogram representation is derived from the GRENOUILLE-recovered electric field from which both the optical spectrum and the optical time trace of the pulse can be intuitively gauged. The results are presented in a unique juxtaposition of the optical spectrum, optical time trace and the spectrogram of both the input and output light pulses. A direct correspondence between peaks in

the spectrum / time-trace and intensity maxima in the spectrogram can be seen. For higher powers, when comparing the experimental and simulated GRENOUILLE traces, it is observed that the frequency resolution and the maximum measurable time-bandwidth product (TBP) of the GRENOUILLE are a limitation. The difference between the effects of self-phase modulation (SPM), and degenerate-cross-phase modulation (DXPM) is indicated and it is shown that the effects of SPM dominate. The method of calculating the beat length of the fiber is described in detail. A possible related practical application, the ability to modulate the light pulses both temporally and spectrally, by passage through such polarization maintaining optical fiber is stated and discussed. The modulation technique is very direct and straightforward. No frequency components of the broadband pulse have to be rejected as the entire spectrum is uniformly modulated. The technique is flexible as the modulation spacing can be varied by varying the fiber length.

5.4 Future Directions

Even though nonlinear pulse propagation through optical fibers has been studied for several decades, there are many interesting open questions remaining in this field. In this section, some of the questions and directions of research relevant to the material covered in the previous chapters are presented.

In chapter 2, the effect of fiber medium inhomogeneities on the sideband evolution was studied, and it was found that the nature of the evolution depended sensitively on the level of the inhomogeneities. This indicated that the four-wave-mixing experiment could be used as a means to determine the level of inhomogeneity

in a given optical fiber. For optical pulses shorter than 1 ps, the same experiment would also involve quantum fluctuations. These too manifest in the NLSE as linear multiplicative noise terms. This indicates that it may be possible to gauge the level of quantum fluctuations using the four-wave-mixing experiment. In the simulations Gaussian white noise was used to represent the fluctuations. If the temporal and spatial correlation properties of the noise are known then the use of colored noise would be more realistic.

In chapter 3, the influence of Raman scattering on four-wave-mixing processes was investigated and it was found that the range of pump power levels and optical fiber lengths considered were lower than those required for Raman scattering to have a visible and appreciable effect. It was observed that for higher powers and longer fiber lengths, the growth of the Raman Stokes wave drastically depletes the pump wave, in a stochastic way. An experimental exploration of this regime of power levels and fiber lengths would be extremely interesting as both four-wave-mixing and Raman scattering would be important. Raman scattering was simulated using two coupled nonlinear Schrodinger equations, one for the pump wave, and one for the Stokes wave. The development of an NLSE based model that includes higher order Stokes wave generation would be an interesting direction of research.

In chapter 4, the effects of self- and cross- phase modulation on asymmetric femtosecond pulses propagating through a polarization maintaining fiber were investigated using GRENOUILLE. Experiments using pulses with controllable asymmetry that could quantify the effects of pulse skewness and kurtosis are directly related to this research. The bandwidth covered by the GRENOUILLE used can

be increased significantly by recently developed methods [58, 59]. It was shown that with a specified length and orientation of the fiber, the light can be modulated to produce pulses with evenly spaced spectral peaks. The spacing and width of the peaks can be varied by varying the fiber length. A flexible WDM (wavelength division multiplexing) source can thus be generated.

All the studies described in this thesis pertain to the normal dispersion regime ($\lambda < \lambda_0$) where λ_0 is the zero-dispersion wavelength. Similar experiments in the anomalous dispersion regime ($\lambda > \lambda_0$), are highly desirable, not only because this is the regime in which bright solitons are possible, but also because this regime contains the least loss wavelength (1.55μm) and the communication wavelengths. The results presented here are for polarization maintaining fiber. Standard single mode fiber are not polarization maintaining, hence it would be interesting to also perform similar experiments with non-polarization maintaining fibers. There are several kinds of fiber available, among them being the dispersion-shifted fiber (DSF), for which the least loss wavelength and zero dispersion wavelength coincide.

BIBLIOGRAPHY

[1] G.P. Agrawal, *Nonlinear Fiber Optics* (Academic Press, San Diego, CA, 2001), Chap. 1.

[2] N. Bloembergen, *Nonlinear Optics* (Benjamin, Reading, MA, 1977).

[3] Y.R. Shen, *Principles of Nonlinear Optics* (Wiley, New York, 1984).

[4] P.N. Butcher and D.N. Cotter, *The Elements of Nonlinear Optics* (Cambridge University Press, Cambridge, UK, 1990).

[5] R.W. Boyd, *Nonlinear Optics* (Academic Press, Sandiego, CA, 1992).

[6] A.C. Newell and J.V. Moloney *Nonlinear Optics(Advanced Topics in the Interdisciplinary Mathematical Sciences)* (Westview Press, Boulder, Colorado, April 1992).

[7] D. Marcuse,*Light Transmission Optics* (Van Nostrand Reinhold, New York, 1982), Chaps. 8 and 12.

[8] G.P. Agrawal, *Nonlinear Fiber Optics* (Academic Press, San Diego, CA, 2001), Chap. 2.

[9] P. Diament, *Wave Transmission and Fiber Optics* (Macmillan, New York, 1990).

[10] V.E. Zakharov and A.Shabat, Sov. Phys. JETP **34**,62(1972)

[11] R.H. Hardin and F.D. Tappert, SIAM Rev. Chronicle **15**,423(1973).

[12] R.A.Fisher and W.K. Bischel, Appl. Phys. Lett. **23**,661(1973); J. Appl. Phys **46**,4921(1975).

[13] J.W. Cooley and J.W. Tukey, Math. Comput. **19**,297(1965).

[14] R. Trebino, D.J. Kane, "Using phase retrieval to measure the intensity and phase of ultrashort pulses: frequency resolved optical gating", J. Opt. Soc. Am. B **10**, 1101 (1993).

[15] D.J. Kane, R. Trebino, "Characterization of Arbitrary Femtosecond Pulses Using Frequency-Resolved Optical Gating", IEEE J. Quant. Elect. **29**, 571 (1993).

[16] D.J. Kane, R. Trebino, "Single-shot measurement of the intensity and phase of an arbitrary ultrashort pulse by using frequency-resolved optical gating", Opt. Lett. **10**, 1101 (1993).

[17] P. O'Shea, M. Kimmel, X. Gu, R. Trebino, "Highly simplified device for ultrashort-pulse measurement", Opt. Lett. **26**, 932 (2001).

[18] G.P. Agrawal, *Nonlinear Fiber Optics* (Academic Press, San Diego, CA, 2001), Chap. 3.

[19] G.P. Agrawal, *Nonlinear Fiber Optics* (Academic Press, San Diego, CA, 2001), Chap. 4.

[20] G.P. Agrawal, *Nonlinear Fiber Optics* (Academic Press, San Diego, CA, 2001), Chap. 10.

[21] G.P. Agrawal, *Nonlinear Fiber Optics* (Academic Press, San Diego, CA, 2001), Chap. 7.

[22] G.P. Agrawal, *Nonlinear Fiber Optics* (Academic Press, San Diego, CA, 2001), Chap. 6.

[23] R.H. Stolen, E.P. Ippen, and A.R. Tynes, Appl. Phys. Lett. **20**, 62(1972).

[24] E.P. Ippen and R.H. Stolen, Appl. Phys. Lett. **21**, 539(1972).

[25] R.G. Smith, Appl. Opt. **11**, 2489(1972)

[26] G.P. Agrawal, *Nonlinear Fiber Optics* (Academic Press, San Diego, CA, 2001), Chap. 9.

[27] G.P. Agrawal, *Nonlinear Fiber Optics* (Academic Press, San Diego, CA, 2001), Chap. 8.

[28] D.L. Hart, Arthur F. Judy, Rajarshi Roy and James W. Beletic, Phys. Rev. E **57**, 4757 (1998), D.L. Hart, Arthur F. Judy, T.A.B. Kennedy, Rajarshi Roy and K. Stoev, Phys. Rev. A **50**, 1807 (1994).

[29] K. Ito, *Lectures on Stochastic Processes* (Tata Institute of Fundamental Research, Bombay, 1960).

[30] R.L. Stratanovich, *Topics in the Theory of Random Noise*, Vols I. and II. (Gordon & Breach, New York, 1963).

[31] H. Risken, *The Fokker-Planck Equation* (Springer-Verlag, Berlin, 1989).

[32] M.J. Werner and P.D. Drummond, J. Comput. Phys. **132**, 312 (1997).

[33] P.D. Drummond and I.K. Mortimer, J. Comput. Phys. **93**, 144 (1991).

[34] S.J. Carter, Phys. Rev. A. **51**, 3274 (1995).

[35] J.R. Thompson and Rajarshi Roy, Phys. Rev. A **43**, 4987 (1991).

[36] W.H. Press, S.A. Teukolsky, W.T. Vetterling and B.P. Flannery, *Numerical Recipes in Fortran: The Art of Scientific Computing* (Cambridge University Press, Cambridge, 1992).

[37] C. Headley, G.P. Agrawal IEEE J. Quantum Electron. **QE-31**, 2058 (1995), C. Headley, G.P. Agrawal J. Opt. Soc. Am. B. **13**, 2170 (1995).

[38] S.H. Perlmutter, M.D. Levenson, R.M. Shelby and M.B. Weisman, Phys. Rev. Lett. **61** 1388, 1988.

[39] F. Kh. Abdullaev, J.H. Hensen, S. Bischoff and M.P. Sorensen, J. Opt. Soc. Am. B. **15**, 2424 (1998),F. Kh. Abdullaev, J.G. Caputo, and Nikos Flytzanis, Phys. Rev E. **50**, 1552 (1994).

[40] William H. Glenn, IEEE J. Quantum Electron. **QE-25**, 1218 (1989).

[41] R. Trebino. *Frequency-Resolved Optical Gating: The Measurement of Ultrashort Laser Pulses* (Kluwer Academic 2002).

[42] G.P. Agrawal *Nonlinear Fiber Optics* (Academic, San Diego, 2001).

[43] J.M. Dudley, X. Gu, L. Xu, M. Kimmel, E. Zeek, P. O'Shea, R. Trebino, S. Coen, R.S. Windeler, "Cross-correlation frequency resolved optical gating analysis of broadband continuum generation in photonic crystal fiber: simulations and experiments", Opt. Express **10**, 1215 (2002).

[44] Q.D. Liu, J.T. Chen, Q.Z. Wang, P.P. Ho, and R.R. Alfano, "Single pulse degenerate-cross-phase modulation in a single-mode optical fiber", Opt. Lett. **20**, 542 (1995).

[45] T. Sylvestre, H. Maillotte, E. Lantz, and D. Gindre "Combined spectral effects of pulse walk-off and degenerate cross-phase modulation in birefringent fibers", Journal of Nonlinear Optical Physics and Materials 6, 313-320 (1997).

[46] Q.D. Liu, L. Shi, , P.P. Ho, R.R. Alfano, R.J. Essiambre, and G.P. Agrawal, "Degenerate cross-phase modulation of femtosecond laser pulses in a birefringent single-mode fiber", IEEE Photon. Tech. Lett. **9**, 1107 (1997)

[47] F.G. Omenetto, B.P. Luce, D. Yarotski and A.J. Taylor, "Observation of chirped soliton dynamics at l= 1.55 mm in a single-mode optical fiber with frequency-resolved optical gating", Opt. Lett. **24**, 1392 (1999).

[48] F.G. Omenetto, Y. Chung, D. Yarotski, T. Shaefer, I. Gabitov and A.J. Taylor, "Phase analysis of nonlinear femtosecond pulse propagation and self-frequency shift in optical fibers", Opt. Commun **208**, 191 (2002).

[49] F.G. Omenetto, J.W. Nicholson, B.P. Luce, D. Yarotski, A.J. Taylor, "Shaping, propagation and characterization of ultrafast pulses in optical fibers", Appl. Phys. B **70**[Suppl.], S143 (2000).

[50] N. Nishizawa and T. Goto, "Experimental analysis of ultrashort pulse propagation in optical fibers around zero-dispersion region using cross-correlation frequency resolved optical gating", Optics Express **8**, 328 (2001).

[51] N. Nishizawa and T. Goto, "Trapped pulse generation by femtosecond soliton pulse in birefringent optical fibers", Opt. Express **10**, 256 (2002).

[52] N. Nishizawa and T. Goto, "Characteristics of pulse trapping by use of ultrashort soliton pulses in optical fibers across the zero-dispersion wavelength", Opt. Express **10**, 1151 (2002).

[53] N. Nishizawa and T. Goto, "Ultrafast all optical switching by use of pulse trapping across zero-dispersion wavelength", Opt. Express **11**, 359 (2003).

[54] , K. Ogawa, M.D. Pelusi, "Characterization of ultrashort optical pulses in a dispersion-managed fiber link using two-photon absorption frequency-resolved optical gating", Opt. Commun. **198**, 83-87 (2001).

simplified device for ultrashort-pulse measurement", Opt. Lett. **26**, 932 (2001).

[55] R.A. Altes, "Detection, estimation, and classification with spectrograms", J. Acoust. Soc. Am. **67**(4), 1232(1980).

[56] A. Christian Silva, "GRENOUILLE - Practical Issues", unpublished.

[57] J. Garduno-Mejia, A.H. Greenaway, and D.T. Reid, "Designer femtosecond pulses using adaptive optics", Opt. Express **11** 2030(2003).

[58] P. O'Shea, M. Kimmel, X. Gu, R. Trebino, "Increased-bandwidth in ultrashort-pulse measurement using an angle-dithered nonlinear-optical crystal", Opt. Express **7**, 342 (2000).

[59] P. O'Shea, M. Kimmel, R. Trebino, "Increased phase-matching bandwidth in simple ultrashort-laser-pulse measurements", J. Opt. B **4**, 44 (2002).

[60] S. Akturk, M. Kimmel, P.O'Shea, R.Trebino, "Measuring pulse-front tilt in ultrashort pulses using GRENOUILLE", Opt. Express. **11**, 491 (2003).

[61] K. J. Blow, D. Wood, "Theoretical Description of Transient Stimulated Raman Scattering in Optical Fibers", IEEE J. Quant. Elect. **25**, 2665 (1989).

[62] R.H. Stolen, J.P. Gordon, W.J. Tomlinson, J.Opt. Soc. Am. B **6**, 1159 (1989).

[63] P.V. Mamyshev and S.V. Chernikov, Sov. Lightwave Commun. **2**, 97 (1992).

[64] C. Headley III, *Ultrafast Stimulated Raman Scattering in Optical Fibers, Ph.D. Thesis, University of Rochester, NY(1995).*